BIOCHEMISTRY
including biophysical chemistry & molecular biology
Article

Biochemistry **2010,** *49,* 8779–8793 8779
DOI: 10.1021/bi101112c

Binding of β-D-Glucosides and β-D-Mannosides by Rice and Barley β-D-Glycosidases with Distinct Substrate Specificities†

Teerachai Kuntothom,[‡,#,▽] Michal Raab,[#,§] Igor Tvaroška,[§] Sebastien Fort,[∥] Salila Pengthaisong,[‡] Javier Cañada,[⊥] Luis Calle,[⊥] Jesús Jiménez-Barbero,[⊥] James R. Ketudat Cairns,[‡] and Maria Hrmova*[,@,●]

[‡]*School of Biochemistry, Institute of Science, Suranaree University of Technology, Nakhon Ratchasima, Thailand,* [§]*Department of Structure and Function of Saccharides, Institute of Chemistry, Center for Glycomics, Slovak Academy of Sciences, Bratislava, Slovak Republic,* [∥]*Centre de Recherches sur les Macromolecules Vegetales, Grenoble, France,* [⊥]*Centro de Investigaciones Biológicas, CSIC, Madrid, Spain, and* [@]*Australian Centre for Plant Functional Genomics, University of Adelaide, Glen Osmond, Australia.* [#]*These authors made equal contributions to this work.* [▽]*Current address: Department of Chemistry, Mahasarakham University, Mahasarakham, Thailand.* [●]*Also affiliated with Institute of Chemistry, Slovak Academy of Sciences, Bratislava, Slovak Republic.*

Received July 12, 2010; Revised Manuscript Received September 7, 2010

ABSTRACT: Predominantly, rice Os3BGlu7 operates as a β-D-glucosidase (EC 3.2.1.21), while barley HvBII acts as a β-D-mannosidase (EC 3.2.1.25). Saturation transfer difference nuclear magnetic resonance (STD NMR) and transferred nuclear Overhauser effect (trNOE) spectroscopy in conjunction with quantum mechanics/molecular mechanics (QM/MM) modeling and docking at the 6-31+G* level were used to investigate binding of S- and O-linked *gluco*- and *manno*-configured aryl-β-D-glycosides to Os3BGlu7 and HvBII. Kinetic analyses with 4-nitrophenyl β-D-thioglucoside (4NP-S-Glc) and 4-nitrophenyl β-D-thiomannoside (4NP-S-Man) indicated that the inhibitions were competitive with apparent K_i constants of 664 and 710 μM for Os3BGlu7 and 95 and 266 μM for HvBII, respectively. The STD NMR and trNOESY experiments revealed that 4NP-S-Glc and 4NP-S-Man bound weakly in $^4C_1$ conformations to Os3BGlu7; 4NP-S-Glc adopted $^3S_5$ ($B_{3,O}$) or $^1S_3$ ($^{1,4}B$) conformations, and 4NP-S-Man preferred $^4C_1$ geometry, when bound to HvBII. The QM modeling and docking, based on GLIDE scores, predicted that 4NP-O-Glc, 4NP-O-Man, and 4NP-S-Man bound preferentially in $^1S_3$ geometries to both enzymes, contrary to 4NP-S-Glc that could also adopt a $^4C_1$ conformation, although in a "flipped-down" ring position. The experimental and computational data suggested that in glycoside recognition and substrate specificity of Os3BGlu7 and HvBII, a combination of the following determinants is likely to play key roles: (i) the inherent conformational and spatial flexibilities of *gluco*- and *manno*-configured substrates in the enzymes' active sites, (ii) the subtle differences in the spatial disposition of active site residues and their capacities to form interactions with specific groups of substrates, and (iii) the small variations in the charge distributions and shapes of the catalytic sites.

The glycoside hydrolase GH1 family includes enzymes with approximately 20 known substrate specificities (*1*), including β-D-glucosidases (EC 3.2.1.21), 6-phospho-β-D-glucosidases (EC 3.2.1.86), β-D-mannosidases (EC 3.2.1.25), β-D-galactosidases (EC 3.2.1.23), β-D-glucuronidases (EC 3.2.1.31), and others (*2*). A detailed examination of the substrate specificity of the barley β-D-glucosidase isoenzyme βII (HvBII) (*3*, *4*), also designated Hvβ Mannos1 (*5*), revealed that it exhibits a marked preference for manno-oligosaccharides and that the rate of hydrolysis increases with the degree of polymerization of both cello- and manno-oligosaccharides (*3*−*6*). Hence, the substrate specificity and action patterns of HvBII are characteristic of an oligosaccharide exohydrolase, rather than of an enzyme with a preference for low-molecular mass cello-oligosaccharides. Similar conclusions were drawn for an Os3BGlu7 β-D-glucosidase from rice (also called BGlu1), although binding energies at individual subsites differ somewhat (*6*, *7*). Both plant enzymes are capable of catalyzing transglycosylation reactions with 4NP-O-Glc[1] (*3*, *4*, *6*, *7*), but not with 4NP-O-Man. The presence of an extended series of subsites in these two plant β-D-glycosidases indicates that their biological

†This work was supported by grants from the Australian Research Council to M.H. and from the Thailand Research Fund (BRG5080007) to J.R.K.C. T.K. was sponsored by The Institute for the Promotion of Teaching Science and Technology of Thailand. M.R. and I.T. are thankful for support from the Science and Technology Assistance Agency under Contract APVV-0607-07. J.C., L.C., and J.J.-B. thank the Ministerio de Ciencia e Innovacion for support (CTQ2009-08536).

*To whom correspondence should be addressed. Telephone: +61 8 8303 7160. Fax: +61 8 8303 7102. E-mail: maria.hrmova@adelaide.edu.au.

[1]Abbreviations: CAZy, Carbohydrate-Active enZymes; DP, degree of polymerization; CORCEMA, Complete Relaxation and Conformational Exchange Matrix; DPFGSE, double pulse field-gradient spin-echo; EA, catalytic nucleophile; EB, catalytic acid/base; ESP, electrostatic potential; GH, glycoside hydrolase; HDO, hydrogen/deuterium water; ISPA, isolated spin-pair approximation; NOEs, nuclear Overhauser effects; PDB, Protein Data Bank; rmsd, root-mean-square deviation; QM/MM, quantum mechanics/molecular mechanics; STD NMR, saturation transfer difference nuclear magnetic resonance; trNOESY, transferred nuclear Overhauser effect spectroscopy; 1D, one-dimensional; 2D, two-dimensional; 3D, three-dimensional; 4NP, 4-nitrophenyl; 4NP-O-Glc, 4-nitrophenyl β-D-glucopyranoside; 4NP-O-Man, 4-nitrophenyl β-D-mannopyranoside; 4NP-S-Glc, 4-nitrophenyl β-D-thioglucopyranoside; 4NP-S-Man, 4-nitrophenyl β-D-thiomannopyranoside.

Published on Web 09/08/2010

functions could lie in the hydrolysis of longer oligosaccharides, possibly derived from cell wall (1,3;1,4)-glucans and (1,4)-β-D-(gluco)mannans (*3*−*6*, *8*).

Substrate hydrolysis in the GH1 family proceeds with retention of anomeric configuration in a two-step double-displacement catalytic mechanism (*9*). The catalytic event advances with participation of a pair of glutamate residues, a catalytic acid/base and a catalytic nucleophile. The exceptions to this rule in the GH1 family are plant myrosinases, for example, that from *Sinapsis alba* (*10*), which do not have proton donors. Most information about the catalytic mechanism of the GH1 β-D-glucosidases has been derived from chemical modification (*11*, *12*), mutagenesis (*13*), molecular modeling (*3*, *14*), or X-ray diffraction studies (e.g., refs *15* and *16*). The catalysts in a range of β-D-glucosidases were determined using mechanism-based inhibitors; e.g., the catalytic nucleophile in the *Agrobacterium* sp. β-D-glucosidase (*17*) and rice Os3BGlu7 (*16*) were identified with 2′,4′-dinitrophenyl 2-deoxy-2-fluoro-β-D-glucoside, while conduritol B epoxide was used with the *Aspergillus wentii* β-D-glucosidase (*18*) and barley HvBII (*3*). In the HvBII enzyme, the two catalytic amino acid residues, Glu179 and Glu386, are positioned near the bottom of the substrate-binding pocket and are separated by approximately 5−6 Å, although it is not clear how the nonreducing end of the substrate is preferably recognized versus the reducing end by the active site residues (*3*). It is also not apparent how the remainder of the substrate dissociates from the active site after glucose is cleaved, to provide sufficient space for the product to diffuse out of the pocket.

Approximately 30 unique three-dimensional (3D) structures or molecular models (*1*) have been reported for the GH1 enzymes that fold into $(\beta/\alpha)_8$ barrel projections. In contrast to the open cleft structures of endohydrolases, plant and microbial β-D-glucosidases align their glycosidic substrate in dead-end funnels (*3*, *19*). The substrates are brought into juxtaposition with the catalytic pairs close to a glycosidic linkage at the nonreducing terminal residue (*8*, *15*, *20*). Much attention has been devoted to dissecting structural features that are responsible for glycon and aglycon substrate specificities in the GH1 group of enzymes (e.g., refs *8*, *12*, *15*, and *20*). However, despite this effort, so far we have not been able to dissect what precise conformations the *gluco*- and *manno*-configured substrates adopt in bound states in the active sites of plant GH1 β-D-glucosidases and β-D-mannosidases, what transition states develop during their catalytic cycles, and what structural determinants underlie the substrate specificities of these two closely related β-D-glycosidases.

One approach that has previously been fruitful for descriptions of hydrolase−glycoside interactions is to use thio analogues that mimic natural substrates (e.g., refs (*21*−*23*)). In the work presented here, we have used the S-linked *gluco*- and *manno*-configured aryl-β-D-glycosides and the GH1 enzymes Os3BGlu7 from rice and HvBII from barley. These enzymes represent two types of β-D-glycosidases with distinct substrate specificities; i.e., these catalysts prefer to hydrolyze β-D-glucosides and β-D-mannosides, respectively (*3*, *4*, *6*, *7*, *24*). But contrary to employing X-ray crystallography as an experimental tool that has been used in the majority of previous studies, here we interchangeably used saturation transfer difference nuclear magnetic resonance (STD NMR) with transferred nuclear Overhauser effect (trNOE) spectroscopy, in conjunction with predictive computational quantum mechanics/molecular mechanics (QM/MM) calculations. The approaches specified above determined that O- and S-linked *gluco*- and *manno*-configured aryl-β-D-glycosides adopted a range of conformations. The resultant data are discussed in relation to the substrate preferences of the Os3BGlu7 and HvBII enzymes.

EXPERIMENTAL PROCEDURES

Materials. 4-Nitrophenyl β-D-glucopyranoside (4NP-O-Glc) and 4-nitrophenyl β-D-mannopyranoside (4NP-O-Man) were obtained from Sigma Chemical Co. (St. Louis, MO), and 4NP-S-Glc and 4NP-S-Man were prepared through the published organo-synthetic procedures for 1-thioglycosides (*25*). The source of all other chemicals was specified elsewhere (*4*, *6*).

Cloning, Heterologous Expression, and Purification. The cDNAs encoding Os3BGlu7 and HvBII were subcloned into the pET32a expression vector encoding a thioredoxin folding partner protein (Novagen, Madison, WI), at the *Nco*I and *Xho*I restriction sites as described previously (*6*). The HvBII and Os3BGlu7 cDNAs encoding mature proteins corresponded to the EU807965 and U28047 sequences, respectively. Protein expression was conducted after chemical transformation in *Escherichia coli* Origami(DE3) cells (Novagen) and selection on Luria-Bertani agar containing 50 μg/mL ampicillin, 15 μg/mL kanamycin, and 12.5 μg/mL tetracycline. The selected clones were induced for 8 h at 20 °C with 0.3 mM isopropyl β-D-thiogalactopyranoside as previously described (*24*). The Os3BGlu7 and HvBII enzymes were synthesized as His_6-tagged fusion proteins that were purified by immobilized metal affinity chromatography using a Talon resin (Invitrogen Life Technologies, Carlsbad, CA). The NH_2-terminal thioredoxin-His tags were removed by digestion with enterokinase (New England Biolabs, Beverly, MA) (*6*, *26*). The recombinant enzymes were reconstituted in 50 mM sodium acetate buffer at their pH optima, i.e., at pH 5.0 for Os3BGlu7 and pH 4.0 for HvBII (*6*, *7*).

Kinetic Constants and Inactivation by Thio Inhibitors. Kinetic constants of Os3BGlu7 and HvBII were determined as previously detailed (*6*). The reaction mixtures contained 0.038−1.5 mM (0.2−3 times the K_m value) 4NP-O-Glc or 0.042−3.81 mM (0.2−3 times the K_m value) 4NP-O-Man, 0.016% (w/v) BSA, and 2−4 pmol (24−48 nM) of Os3BGlu7 or HvBII in 50 mM sodium acetate buffer at pH 5.0 or 4.0, respectively. The enzyme inactivation constants were determined using 0−600 μM 4NP-S-Glc or 4NP-S-Man. Each inhibitor was tested at four concentrations that were 0.4−3 times the individual K_i (dissociation constant of the enzyme−inhibitor complex) values. The reactions were developed with 2 M Na_2CO_3, and the amount of 4-nitrophenol (4NP) released was measured in microtiter plates using a PolarStar Optima Plate Reader (BMG LabTech, Offenburg, Germany). The enzyme activity was monitored at 405 nm, and the K_i values were determined from Dixon plots (inhibitor concentrations vs $1/v$). Substrate hydrolyses during incubations never exceeded 10% of their initial concentrations, and kinetic constants were determined in triplicate at 30 °C. Hydrolytic and inhibition parameters were calculated by nonlinear regression of the Michaelis−Menten curves with Grafit version 5.0 (Erithacus Software, Horley, Surrey, U.K.).

STD NMR. STD NMR experiments were performed in a phosphate buffer of two different pH values as specified below (D_2O, uncorrected for isotope effects), between 290 and 300 K without saturation of a residual HDO (hydrogen/deuterium water) signal at 4NP-S-Glc or 4NP-S-Man to enzyme molar ratios between 20:1 and 50:1. A train of Gaussian-shaped pulses of 50 ms for each measurement was employed, with a total saturation time of the protein envelope of 2 s and a maximum B1

field strength of 50 Hz. An off-resonance frequency (δ) of 40 ppm and an on-resonance frequency (δ) of −1.0 ppm (protein aliphatic signal region) were applied. In all cases, the line broadening of inhibitor protons was monitored. In each case, the intensities were normalized with respect to the strongest response, which always corresponded to one of the H2 protons. The STD NMR experiments were repeated twice and the results averaged.

For the nuclear Overhauser effects (NOEs) in free states, selective experiments that employed a double-pulse field-gradient spin-echo (DPFGSE) module were conducted. NOE intensities were normalized with respect to the diagonal peak at zero mixing time. Selective T_1 measurements were performed on anomeric and several other protons to obtain the values mentioned above. Experimental NOEs were fitted to the double-exponential function $f(t) = p_0(e^{-p_1 t})(1 - e^{-p_2 t})$, as described previously (*27*, *28*), where p_0, p_1, and p_2 are adjustable parameters. The initial slope was determined from the first derivative at time zero [$f(0) = p_0 p_2$]. Interproton distances were obtained from the initial slopes by employing the isolated spin-pair approximation (ISPA).

The trNOESY experiments with HvBII were performed with freshly prepared mixtures containing HvBII and 4NP-S-Glc or 4NP-S-Man inhibitors, at approximately 30:1 molar ratios, in 20 mM phosphate buffer (pH 5.0) (near the pH optimum), with mixing times of 50, 100, 150, and 200 ms (*28*), resulting in final thio inhibitor concentrations of approximately 2−3 mM. No purging spin-lock period was employed to remove the NMR signals arising from the HvBII background, because typically the background signals are not observed with large proteins such as HvBII. First, line broadening of the inhibitor protons was monitored after the addition of the enzyme. The theoretical analysis of the trNOEs of 4NP-S-Glc or 4NP-S-Man protons was performed using Complete Relaxation and Conformational Exchange Matrix (CORCEMA), and a relaxation matrix with exchange as described previously (*28*). Varying exchange rate constants were employed to obtain optimal matches between the experimental and theoretical results of the methylene protons of 4NP-S-Glc or 4NP-S-Man at the C6 atoms, which could be separated by a fixed distance of 1.8 Å. The overall correlation time (τ_c) for the free states of inhibitors was always set to 50 ps for the monosaccharides, while τ_c was set to 10 ns for bound states. To fit the experimental trNOE intensities, off-rate constants between 100 and 1000 s^{-1} were tested. An optimal agreement was achieved for a k_{off} of 100−300 s^{-1}.

Interactions of Os3BGlu7 with 4NP-S-Glc and 4NP-S-Man were investigated as described above, except that 20 mM Tris-HCl buffer (pH 8.0) or 20 mM phosphate buffer (pH 6.0) (near the pH optimum) was used, to avoid protons in NMR spectra in the latter case. The other experimental details used were as specified for HvBII.

All spectra were recorded between 290 and 300 K on a Bruker AVANCE 500 MHz spectrometer, equipped with a triple-channel ^1H, ^{13}N, ^{15}N gradient probe and processed with the Topspin Bruker software.

Homology Modeling of HvBII. A rice β-D-glucosidase Os3BGlu7 [PDB entry 2RGL (*16*)] was used as a structural template. The template sequence was aligned with that of HvBII using ClustalW (*29*), and the alignment was checked manually to maintain the integrity of secondary structure elements (*30*). The levels of sequence similarity and identity between HvBII and 2RGL were 92 and 66%, respectively. The structurally aligned sequences were used as input parameters to generate 200 models of HvBII with Modeler 9v2 (*31*). The top five models with the lowest value of the Modeler 9v2 Objective Function were assessed by the DOPE module of Modeler 9v2, and the model with the most favorable value was chosen for evaluation. The overall *G* factors (estimates of stereochemical parameters) in both coordinate files, assessed by PROCHECK (*32*), were 0.31 and 0.04 for 2RGL and HvBII, respectively, with 99.8 and 0.2% of the residues in the favored, additional, and generously allowed regions and disallowed regions, respectively. WHATIF (*33*) evaluated the packing environment in the structures and returned quality control values of −0.97 and −0.77 for 2RGL and HvBII, respectively, while Verify 3D (*34*), which scores the fitness of protein sequences in their 3D environment, showed that 98.3% (2RGL) and 97.7% (HvBII) of the residues had an acceptable 3D−1D score. The *z* score values (*35*) reflecting combined statistical potential energy for 2RGL and HvBII were −11.59 and −12.38, respectively. The rmsd value in the Cα positions between the model and its template was 0.147 Å over 470 residues, from a total of 474 and 479 residues in 2RGL and HvBII, respectively, as determined with Stamp (*36*). Surfaces of Os3BGlu7 and HvBII were calculated with PyMol (*37*) with a probe radius of 1.4 Å, electrostatic potentials with the Adaptive Poisson−Boltzmann Solver (the dielectric constants of the solvent and solute were 80 and 2, respectively) (http://apbs.sourceforge.net/) implemented in PyMol as a plugin, and mapped on the protein molecular surfaces. The overall buriedness parameters of the HvBII and 2RGL active site funnels were calculated by the PocketPicker plugin (*38*) in PyMol. Molecular graphics were generated with PyMol and the Maestro graphical interface within the Schrödinger software suite (*39*).

Computational Docking of 4NP-O- and 4NP-S-Glycosides. Twelve starting structures for 4NP-Glc, 4NP-Man, 4NP-S-Glc, and 4NP-S-Man were constructed (*39*). For 1-O- and 1-S-gluco- and -mannopyranosides, three ring conformations were considered, namely, $^1S_3$ ($^{1,4}B$) (1B, 2B, 3B, and 4B), $^3S_5$ ($B_{3,O}$) (1S, 2S, 3S, and 4S), and $^4C_1$ (1C, 2C, 3C, and 4C). All 12 structures were fully optimized using the DFT/M05-2X method (*40*−*42*) at the 6-31+G* basis. The electrostatic potential (ESP) charges fitted to the atom centers were calculated at the same level of theory that was used for the optimized structures. Calculations were conducted using Jaguar (*39*).

The 12 optimized structures of β-D-glycosides were docked in the active sites of the crystal structure of Os3BGlu7 (PDB entry 2RGM) and the HvBII model. The preparation of proteins for docking consisted of the following steps. First, both protein structures were reduced to single monomeric units, and water and bound inhibitor molecules were removed. The protein preparation utility within the Schrödinger suite was used to add hydrogen atoms, explicitly define disulfide linkages, and assign protonation states of residues. The structures of both proteins were minimized through 1000 cycles with MacroModel (*39*) using the OPLS-AA force field (*43*). The last structures from minimizations were selected for the calculation of the ESP charges for the residues in the active sites utilizing the hybrid QM/MM approach, as implemented in the QSite subroutine (*39*). For this purpose, the DFT/M05-2X method with the lacvp basis set was used for calculations, over the QM region that consisted of residues within an ~4 Å radius around the −1 subsite. The MM part contained the remainder of the proteins that were treated with an OPLS-AA all-atom force field approximation. The QM/MM boundaries were treated with a hydrogen capping approach. Both proteins were assigned charges from the QM/MM calculations that were used to construct the grid models for docking. The docking sites

Table 1: Kinetic Constants for Hydrolysis and Inhibition by Os3BGlu7 and HvBII

	K_m[a] (mM)	k_{cat}[a] (s^{-1})	$k_{cat}K_m^{-1}$[b] (s^{-1} mM^{-1})	K_i (μM)	ΔG[c] (kJ mol^{-1})
Os3BGlu7					
4NP-O-Glc	0.23 ± 0.02	7.90 ± 0.4	35.1 ± 1.0		
4NP-O-Man	1.30 ± 0.1	1.32 ± 0.05	1.01 ± 0.02		
4NP-S-Glc				664.3 ± 64.4	−18.4
4NP-S-Man				710.3 ± 115.1	−18.3
HvBII					
4NP-O-Glc	0.50 ± 0.03	0.50 ± 0.07	1.0 ± 0.05		
4NP-O-Man	0.25 ± 0.01	3.10 ± 0.02	12.7 ± 0.2		
4NP-S-Glc				94.7 ± 16.8	−23.3
4NP-S-Man				265.9 ± 57.2	−20.7

[a]Rounded to a single decimal digit, when higher than 1.0. [b]Data from refs *6* and *7*. [c]Calculated according to the equation $\Delta G = -RT \ln(1/K_i)$ (*59*).

were restricted to a cube with a 12 Å radius around the active site; no additional constraints were defined, and all 12 β-D-glycosides structures were docked into the active sites of both enzymes. The GLIDE program from the Schrödinger suite (*39*, *44*) was used to calculate and evaluate descriptors for docking fitness. The resultant complexes were inspected for proper orientations and distances of bound substrates with respect to the corresponding active site residues.

RESULTS

Kinetic Parameters for Inhibition by β-D-Thioglycosides. The parameters K_i and ΔG resulting from measurements of inhibition kinetics of rice Os3BGlu7 and barley HvBII with 4NP-S-Glc and 4NP-S-Man are listed in Table 1. The values of the K_i constants varied between 95 and 710 × 10^{-6} M with both enzymes, and the thioglycosides exhibited competitive-type inhibition (data not shown). Hence, the $v = (V_{max}S)/[K_m(1 + I/K_i) + S]$ equation was used for calculations of K_i constants. The ΔG values of inactivation for HvBII with 4NP-S-Glc and 4NP-S-Man were approximately 2−5 kJ/mol more favorable than the respective values for Os3BGlu7. This difference represented a small but significant variation between the two enzymes (Table 1). Table 1 also contains the k_{cat} and K_m values for hydrolysis of 4NP-O-Glc and 4NP-O-Man that were previously determined (*4*, *6*, *7*), but for comparison to our work, these constants are included. The catalytic efficiency factor for Os3BGlu7 with 4NP-O-Glc was ~35-fold higher than that for 4NP-O-Man (*6*, *7*), while for HvBII, this second-order rate constant ($k_{cat}K_m^{-1}$) was ~13-fold higher with 4NP-O-Man than with 4NP-O-Glc (Table 1).

STD and trNOESY NMR Investigations. As a first step, the conformations of free thio inhibitors 4NP-S-Glc and 4NP-S-Man were investigated (Figure 1). The analysis of vicinal proton−proton coupling constants permitted deduction of the exclusive existence of $^4C_1$(D) chair conformations for both inhibitors in solution, as expected. In these cases, NOE experiments were performed to measure the cross relaxation rates that could be correlated with interproton distances. Positive NOEs were obtained at a variety of mixing times from 200 to 1000 ms (Figure 1), as expected for small molecules that display fast tumbling in solution. Excellent agreement was found between the experimentally estimated distances from NOE signals and those measured for the MM3*-minimized $^4C_1$(D) 4NP-S-Glc and 4NP-S-Man chair geometries (data not shown).

The STD NMR experiments with HvBII permitted the unambiguous deduction of that the enzyme recognized both inhibitor molecules, because clear STD signals were observed for all the protons in 4NP-S-Glc and 4NP-S-Man (Figure 2; the data shown for 4NP-S-Glc). Because of the small size of the thio inhibitors, a clear quantitative definition of the inhibitor epitopes was not attempted, as it was expected that the entire ring of thioglycosides would be recognized by HvBII. Here, a small transfer of saturation to the hydroxymethyl protons was observed with

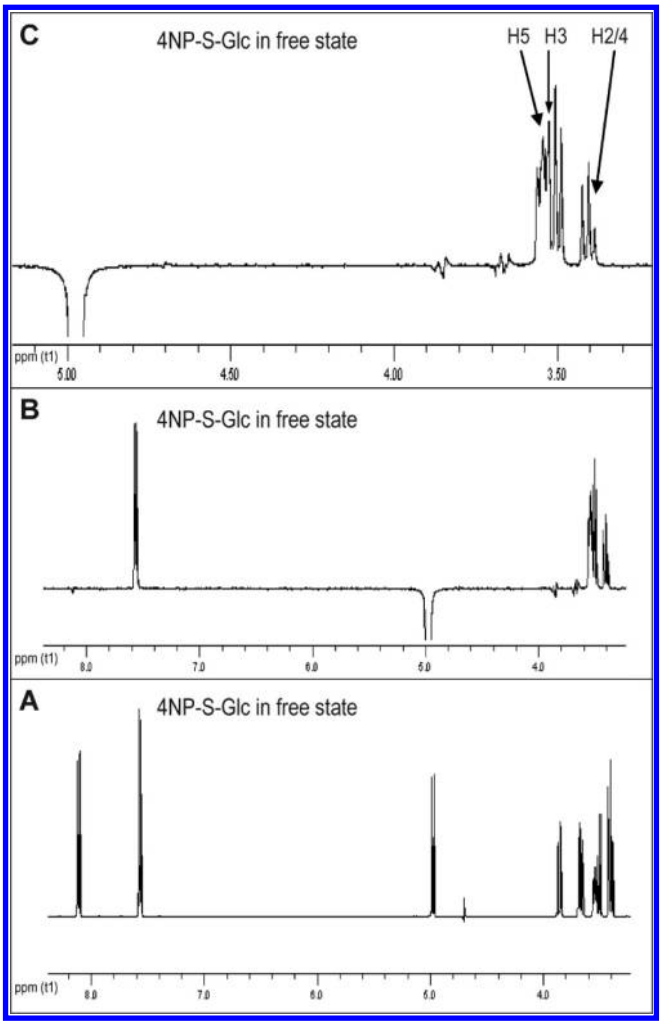

FIGURE 1: Nuclear Overhauser effects observed for free 4NP-S-Glc. (A) The 500 MHz NMR spectrum of 4NP-S-Glc in a free state. Overlapping of H2 and H4 occurs at the high field signal (δ 3.40). (B) NOE enhancements (mixing time of 600 ms) measured upon inversion of an anomeric signal (δ 4.98). Positive NOEs at the ortho-4NP, H5, H3, and H2/4 protons are clearly observed. (C) Expansion of the ring sugar protons, showing that the signal for the H1−H5 NOE was slightly larger than that for the H1−H3 proton pair. The latter pair was significantly larger than that for the H1−H2/4 proton pair. The observations were valid for all mixing times between 200 and 1000 ms.

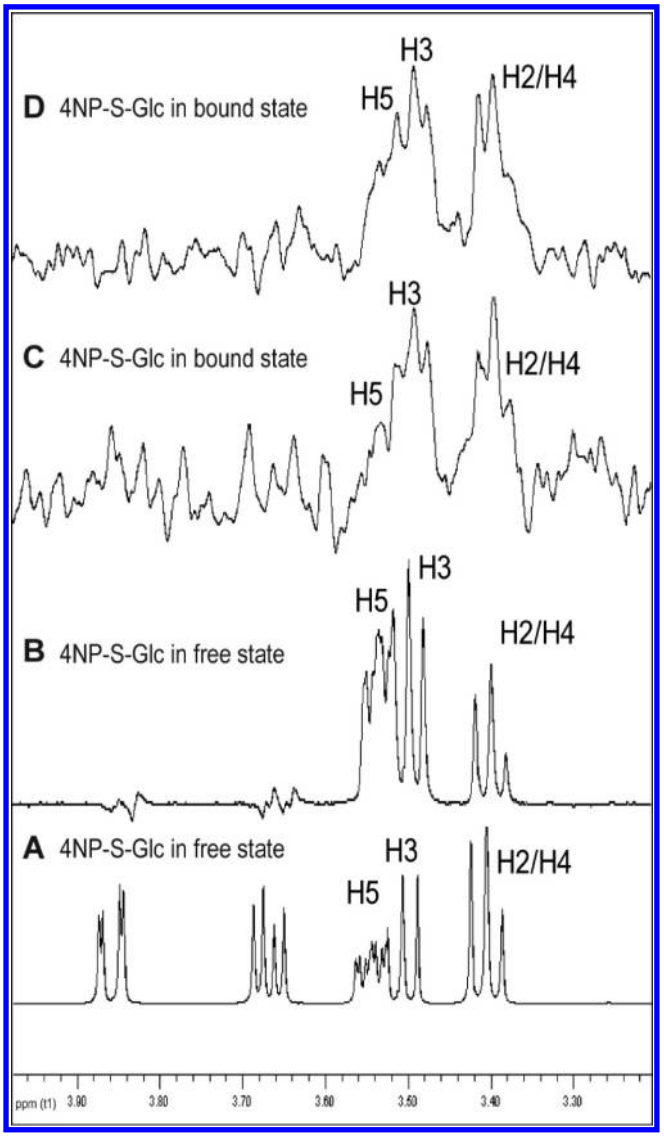

FIGURE 2: Binding of 4NP-S-Glc to HvBII. (A) The 500 MHz NMR spectrum of 4NP-S-Glc in the free state. The arrows indicate the positions of the H1−H5, H1−H3, and H1−H2/4 proton pairs. The overlapping of H2 and H4 occurred at a high field signal (δ 3.40). (B) Section of the NOESY spectrum showing the NOE enhancements (mixing time of 600 ms) measured upon inversion of the anomeric signal of free 4NP-S-Glc (δ 4.98). Positive NOEs at the H1−H5, H1−H3, and H1−H2/4 proton pairs were observed. The NOE signal for the H1−H5 proton pair was slightly larger than that for the H1−H3 proton pair, which was significantly larger than that for the H1−H2 proton pair. (C) Section of the trNOESY spectrum (4NP-S-Glc:HvBII molar ratio of 30:1, mixing time of 100 ms) showing the trNOE enhancements measured upon inversion of the anomeric signal of free 4NP-S-Glc (δ 4.98). (D) Negative NOEs at the H1−H3 and H1−H2/4 proton pairs. The signal for the H1−H5 proton pair was weaker and the signal for the H1−H3 proton pair similar to that of the H1−H2/4 proton pair.

both thio inhibitors, while strong STD signals were observed for the 4NP protons, indicating that this moiety also binds to the HvBII active site (Figure 2A,B; the data shown for 4NP-S-Glc).

Further, strong and negative trNOESY cross-peaks were observed for both inhibitors at a 30:1 ligand:enzyme molar ratio (Figure 2C) with the 100 ms NOE mixing time, as well as at other regimes of 50−200 ms (data not shown). The data for 4NP-S-Glc contrasted with those of 4NP-S-Glc in a free state, where the NOE cross-peaks were positive (cf. Figures 1 and 2). This change from positive to negative cross-peaks upon addition of the enzyme again indicated binding and that, importantly, these trNOESY experiments could be used to deduce the conformations of bound 4NP-S-Glc and 4NP-S-Man. A CORCEMA-based full-relaxation matrix analysis of the cross-peaks was performed to deduce the experimental proton−proton distances in the bound state, and these cross-peaks were then compared with those that were estimated for all possible chair and skew boat conformers of both inhibitors (Table S1 of the Supporting Information). It was evident that for 4NP-S-Glc, the relative cross-relaxation rates (σ) were rather different from those observed in a free state. Here, the σ values were measured for the H1−H2 pair (σ_{12}), and the data indicated that these values were similar to σ_{13} but were larger than σ_{15} (Table S1 of the Supporting Information). These observations contrasted with those obtained for free 4NP-S-Glc. In this case, σ_{15} was larger than σ_{13}, which in turn was 2-fold larger than σ_{12}. On the basis of these data, we concluded that, in the state bound to HvBII, 4NP-S-Glc could adopt a geometry for which the interproton H1−H2 distance was similar to the H1−H3 distance but was shorter than that between the H1 and H5 protons. These analyses suggested that a conformational change of the six-member ring of 4NP-S-Glc had occurred upon binding to HvBII, and thus, the 4NP-S-Glc inhibitor in the bound state no longer adopted a $^4C_1$ chair conformation (Table S1 of the Supporting Information).

In contrast, 4NP-S-Man bound to HvBII had very similar relative cross-relaxation rates for the key proton pairs σ_{12}, σ_{13}, and σ_{15} (Table S2 of the Supporting Information). Essentially, identical cross-relaxation rates were observed for both free and bound states, although they had different signs, a negative one for a bound state and a positive one for a free state. This quantitative data suggested that, in principle, no changes in the interproton distances occurred in 4NP-S-Man, when bound to HvBII, and thus no significant conformational geometry changes from the ground $^4C_1$ conformation occurred during the molecular recognition by HvBII (Table S2 of the Supporting Information).

The nature of the distortion of the pyranose ring of 4NP-S-Glc upon binding to HvBII was assessed by comparison of the experimental interproton distances of bound 4NP-S-Glc with those measured in the MM3*-minimized geometries of the pseudorotational itinerary of 4NP-S-Glc. Here, we considered two extreme chair geometries, $^4C_1$(D) and $^1C_4$(D), and five skew boat conformers, $^0S_2$, $^1S_3$, $^3S_5$, $^4S_0$, and $^1S_5$. Obviously, a chair conformation could not explain the observed NOE enhancements and the corresponding cross-relaxation rates (Table S1 of the Supporting Information). The best match between the observed and computed distances was found for the $^3S_5$ skew boat conformer (Table S1 of the Supporting Information and Figure 3A), although given that there were intrinsic uncertainties for the trNOESY experiments and for the conversion of the cross-relaxation rates into distances, the existence of the $^1S_3$ geometry for bound 4NP-S-Glc could not completely be excluded (Figure 3B). It was characteristic to observe that, for the $^3S_5$ and $^1S_3$ geometries, the anomeric C−S bond adopted a pseudoaxial orientation with a proper orientation for the aglycone moiety to depart. The same pseudoequatorial arrangement was also adopted by the hydroxyl groups at the C2, C3, and C4 atoms of the glucose ring. The major difference between the $^1S_3$ and $^3S_5$ conformers of 4NP-S-Glc is in the orientation of the C6 hydroxymethyl group, which is pseudoaxial for the $^3S_5$ conformer and pseudoequatorial for the $^1S_3$ geometry (Figure 3A,B).

The analogous STD NMR and trNOESY analyses for 4NP-S-Man showed that no major distortion occurred upon binding

to HvBII, because the estimated interproton distances were in full agreement with those computed for the $^4C_1$(D) chair conformer (Figure 3C). Our findings indicated that the data obtained for 4NP-S-Man could function as an "additional internal reference point" for validating the conclusions deduced for the conformational changes of bound 4NP-S-Glc, given that both experiments were performed under identical experimental conditions.

The STD experiments with Os3BGlu7 interacting with 4NP-S-Glc provided weak transferred signals (data not shown). These experiments proceeded in 20 mM Tris-HCl buffer at a pH value of 8.0 that was similar to the pH value at which the crystal structure of Os3BGlu7 was determined [PDB entry 2RGL (*16*)]. A high magnetization transfer was observed only for the aromatic ring protons, while the peaks in the carbohydrate part of 4NP-S-Glc were barely visible. Also, the two-dimensional (2D) trNOESY method did not provide cross-peaks for the 4NP-S-Glc bound to Os3BGlu7 at a molar ratio of 20:1 or 50:1. We have further investigated 1D selective NOESY on H1 of the glucose residue using different mixing times; however, no NOESY peaks were observed in the carbohydrate or aromatic regions of the spectra (data not shown). Hence, we concluded that a rather weak binding of 4NP-S-Glc to OS3BGlu7 could be responsible for a lack of measurable signals. These conclusions were supported by the weak K_i constant (664 μM) for binding of 4NP-S-Glc to Os3BGlu7 (Table 1).

One of the reasons that explains why we did not detect the measurable NOE signals with Os3BGlu7 and 4NP-S-Glc at pH 8.0 could be that at this particular pH value, the enzyme's affinity for the thio inhibitor could be low. Hence, the measurements were repeated at pH 6.0 in 20 mM phosphate buffer, whereas under these conditions, the pH value was closer to the pH optimum of 5.0 of Os3BGlu7 (*7*). Nevertheless, under these conditions, Os3BGlu7 unexpectedly hydrolyzed 4NP-S-Glc to a small extent, as evidenced by the appearance of new spectral peaks that corresponded to hydrolytic products of 4NP-S-Glc (data not shown). Hence, it could be concluded that with Os3BGlu7, 4NP-S-Glc should be cautiously used as a substrate mimic for investigations of binding interactions.

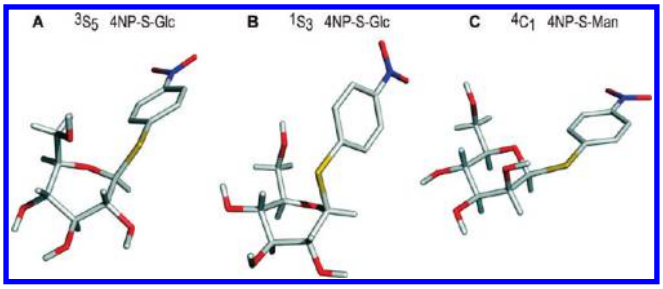

FIGURE 3: Geometries of 4NP-S-Glc and 4NP-S-Man bound to HvBII, as identified by STD NMR. 4NP-S-Glc is shown in the $^3S_5$ (A) and $^1S_3$ (B) conformations, while 4NP-S-Man is in the $^4C_1$ conformation (C).

To investigate binding of 4NP-S-Man to Os3BGlu7, the experimental approach used for binding of 4NP-S-Glc to Os3BGlu7 was adopted, where we first used 20 mM Tris-HCl buffer (pH 8.0) and then 20 mM phosphate buffer (pH 6.0). The STD and transferred NOESY experiments conducted at pH 8.0 with 4NP-S-Man and Os3BGlu7 produced better signals at a molar ratio of 50:1 than at 20:1 (data not shown). A major saturation transfer was again observed on the aromatic protons, followed by the H1 and H2 protons of the mannosyl residue (data not shown). As indicated in Figure 4, in 20 mM phosphate buffer (pH 6) using 1D selective trNOESY conditions, the cross-peaks from H1 to H2, H3, and H5 exhibited the same intensity, as seen for the free inhibitor. These data suggested that no major distortion of the mannosyl $^4C_1$ chair ring had occurred.

QM Modeling and Docking Simulations. The geometry optimizations of the starting $^1S_3$, $^3S_5$, and $^4C_1$ conformers of the O- and S-linked 4NP-Glc and 4NP-Man were conducted at the M05-2X/6-31+G* level of theory, and the calculations yielded the β-D-glycoside conformers in their local minima (Figure 5). The optimized values of selected bond lengths, bond angles, and dihedral angles and ESP partial charges of conformers are summarized in Table S3 of the Supporting Information. A comparison of the structural features of the O- and S-linked 4NP-Glc and 4NP-Man conformers revealed that the glycosides displayed the following structural characteristics. The ESP partial charge on the anomeric carbon of the O-linked glycosides was less negative than the charges on the S-linked glycosides, ranging from 0.36 to 0 for the O-linked versus 0.05 to −0.51 for the S-linked glycosides. Further, the ESP charge on the glycosidic linkage atoms was less negative for the S-linkage (−0.01 to −0.24) than for the O-linkage (−0.29 to −0.54). The partial charge of the endocyclic oxygen was similar for both types of glycosides (−0.36 to −0.53 and −0.22 to −0.40 for the O- and the S-linked glycosides, respectively). The lengths of the C1−O1 linkages in the O-linked glycosides were approximately 0.4−0.5 Å shorter than the lengths of the C1−S1 linkages. Hence, the distances in the O-linked glycosides were between 1.41 and 1.44 Å, while the same distances in the S-linked glycosides were between 1.85 and 1.92 Å (Table S3 of the Supporting Information). The same trend was observed for the lengths of the O1−C7 linkages, which were shorter by approximately 0.44 Å than the lengths of the S1−C7 linkages (Table S3 of the Supporting Information). The calculated C1−X1−C7 angles

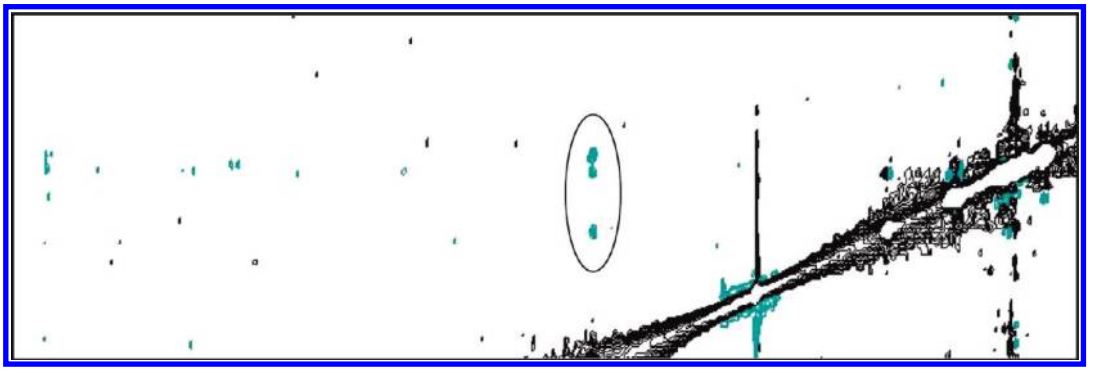

FIGURE 4: Binding of 4NP-S-Man to Os3BGlu7 at a molar ratio of 10:1. In the 2D spectrum, the circled cross-peaks between the anomeric proton and the H2, H3, and H5 protons of 4NP-S-Man showed similar intensities, suggesting that the glycoside was bound in the $^4C_1$ conformation.

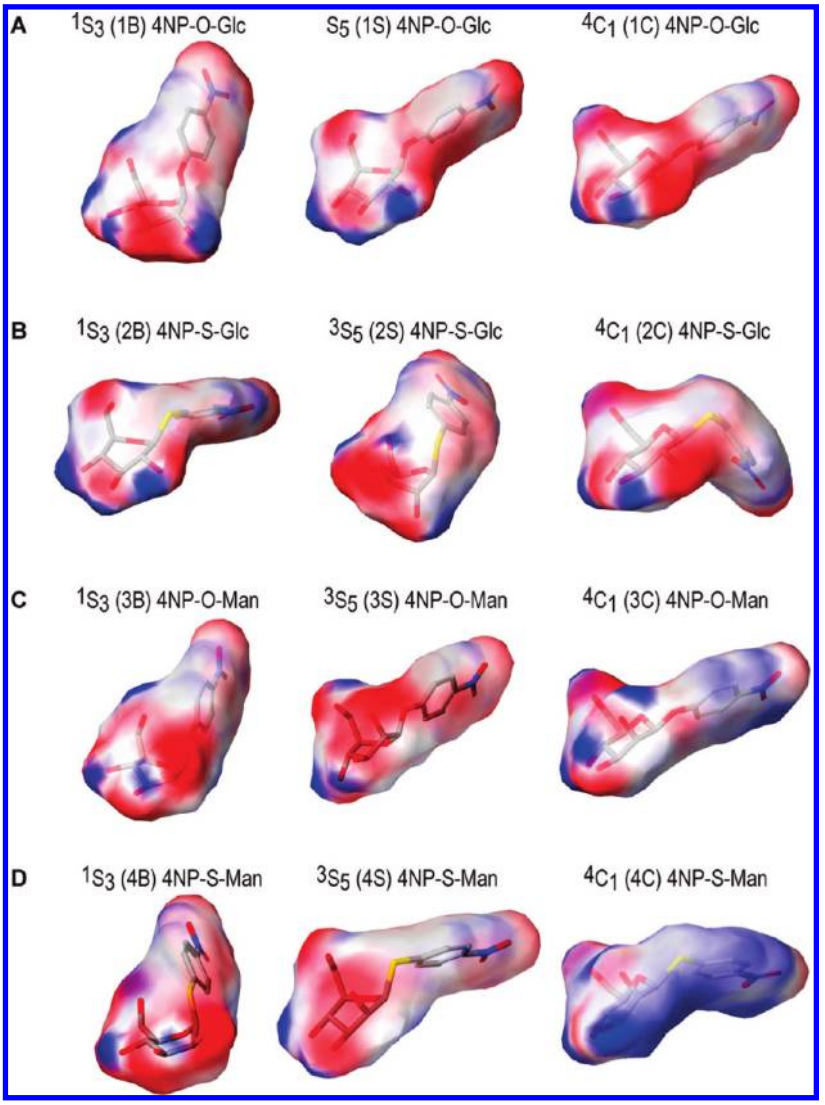

FIGURE 5: Optimized pyranose ring conformations of the *gluco*- and *manno*-configured aryl-glycosides in their local minima that were used for docking: (A) 4NP-O-Glc in $^1S_3$ (1B), $^3S_5$ (1S), and $^4C_1$ (1C); (B) 4NP-S-Glc in $^1S_3$ (2B), $^3S_5$ (2S), and $^4C_1$ (2C); (C) 4NP-O-Man in $^1S_3$ (3B), $^3S_5$ (3S), and $^4C_1$ (3C); and (D) 4NP-S-Man in $^1S_3$ (4B), $^3S_5$ (4S), and $^4C_1$ (4C). The contours denote surfaces and their electrostatic potentials derived from the ESP charges.

of the glycosidic linkages also varied significantly, whereby the C1−S1−C7 bond angles were sharper by as much as 21−30° than the C1−O1−C7 angles. The values were between 87° and 95° for the C1−S1−C7 angle and between 116° and 118° for the C1−O1−C7 angle (Table S3 of the Supporting Information). The minima around the C1−X1 linkages of all aryl-glycoside conformers, predefining their dihedral angles Θ, Φ, and Ψ, corresponded to the synclinal (sc) orientations of the phenyl groups with respect to the pyranose rings, and to the antiperiplanar (ap) orientations at the C2 atoms, in agreement with the exoanomeric effect (*45*).

Twelve optimized aryl-glycosides in $^1S_3$, $^3S_5$, and $^4C_1$ geometries, that is, 4NP-O-Glc in 1B, 1S, and 1C, 4NP-S-Glc in 2B, 2S, and 2C, 4NP-O-Man in 3B, 3S, and 3C, and 4NP-S-Man in 4B, 4S, and 4C, were docked in the active sites of Os3BGlu7 and HvBII, using GLIDE (Table 2 and Figures 6−8). As expected for a *gluco*-O-configured aryl-glucoside, the $^1S_3$ conformer, also known as the $^{1,4}B$ (1B) skew boat conformer, fitted most favorably in Os3BGlu7 and HvBII, as supported by the GLIDE score values of −7.2 kcal/mol in both instances; these scores were the highest from all conformers for both enzymes (Table 2). The predicted affinities for the $^3S_5$ conformer, also known as $B_{3,O}$ (1S) and $^4C_1$ (1C) conformers of 4NP-O-Glc, were between −5.2 and −6.0 kcal/mol for Os3BGlu7 and HvBII (Table 2). However, a similar GLIDE score value was predicted for the $^1S_3$ (2B) (−6.7 kcal/mol) and $^4C_1$ (2C) (−6.8 kcal/mol) conformers of 4NP-S-Glc docked in Os3BGlu7. Here the difference between the $^1S_3$ and $^4C_1$ conformers of 4NP-S-Glc was smaller than the precision of the scoring function. Therefore, on the basis of the GLIDE scores, we concluded that the $^1S_3$ (2B) or $^4C_1$ (2C) conformers of 4NP-S-Glc could equally be fitted in Os3BGlu7 (Table 2). On the other hand, for 4NP-S-Glc bound to HvBII, the higher scores were predicted for the $^1S_3$ and $^4C_1$ conformers (−5.8 and −5.7 kcal/mol, respectively) than for the $^3S_5$ conformer (−4.9 kcal/mol). Similarly, for the *manno*-configured aryl-glycosides, the best predicted score values were obtained for the $^1S_3$ conformations. In the case of 4NP-O-Man in $^1S_3$ (3B), the binding to Os3BGlu7 was slightly more favorable than that to HvBII, with scores of −7.3 kcal/mol versus −6.9 kcal/mol, while 4NP-O-Man in the $^3S_5$ and $^4C_1$ conformers bound less favorably, with affinities of −6.3 kcal/mol for Os3BGlu7 versus −5.6 kcal/mol for HvBII, and −5.5 kcal/mol for Os3BGlu7 versus −5.4 kcal/mol for HvBII (Table 2). The predicted affinities for 4NP-S-Man

Table 2: Summary of Docking of 4NP-O-Glc ($^1S_3$, $^3S_5$, and $^4C_1$ or 1B, 1S, and 1C), 4NP-S-Glc ($^1S_3$, $^3S_5$, and $^4C_1$ or 2B, 2S, and 2C), 4NP-O-Man ($^1S_3$, $^3S_5$, and $^4C_1$ or 3B, 3S, and 3C), and 4NP-S-Man ($^1S_3$, $^3S_5$, and $^4C_1$ or 4B, 4S, and 4C) in Os3BGlu7 and HvBII, Illustrating the Relative Conformational "Strain" Energy (ΔE) of Docked Conformers at the M05-2X/6-31+G* Level of Theory

	GLIDE score		d^a (C1···O_{EA}[b])		d^a (O1/S1···O_{EB}[b])		d^a (HO_2···O_{EB}[b])		strain energy (ΔE^a)	
	Os3BGlu7	HvBII	Os3BGlu7	HvBII	Os3BGlu7	HvBII	Os3BGlu7	HvBII	Os3BGlu7	HvBII
1B	−7.24	−7.15	3.19	2.89	3.64	3.42	1.61	3.20	17.21	18.31
1S	−6.02	−5.34	3.51	3.33	3.47	3.16	1.60	1.46	30.90	22.72
1C	−5.82	−5.20	5.13	5.02	4.38	4.02	7.27	3.39	24.05	16.45
2B	−6.66	−5.77	4.67	4.66	4.32	4.03	4.37	3.14	26.30	26.83
2S	−6.43	−4.86	4.64	3.48	3.40	3.37	7.08	1.50	26.58	33.80
2C	−6.76	−5.74	3.84	4.82	4.37	4.90	7.25	3.85	23.30	24.29
3B	−7.28	−6.89	3.33	3.00	4.22	3.69	4.10	3.01	30.44	26.10
3S	−6.33	−5.57	3.87	3.40	3.89	3.23	4.49	3.12	21.21	14.84
3C	−5.51	−5.36	4.39	4.92	3.51	3.87	4.28	2.46	25.61	21.80
4B	−7.56	−7.26	3.10	2.95	3.59	3.27	1.47	1.56	15.31	22.46
4S	−5.97	−5.70	4.96	4.40	3.13	4.46	4.21	5.20	26.39	15.66
4C	−6.61	−5.68	4.42	4.72	5.93	3.14	5.01	1.70	27.35	26.38

[a]Lengths (d) in angstroms and GLIDE scores and strain energies (ΔE) in kilocalories per mole. [b]EA denotes the catalytic nucleophile residues Glu386 in Os3BGlu7 and Glu389 in HvBII, and EB denotes the catalytic acid/base residues Glu176 in Os3BGlu7 and Glu179 in HvBII.

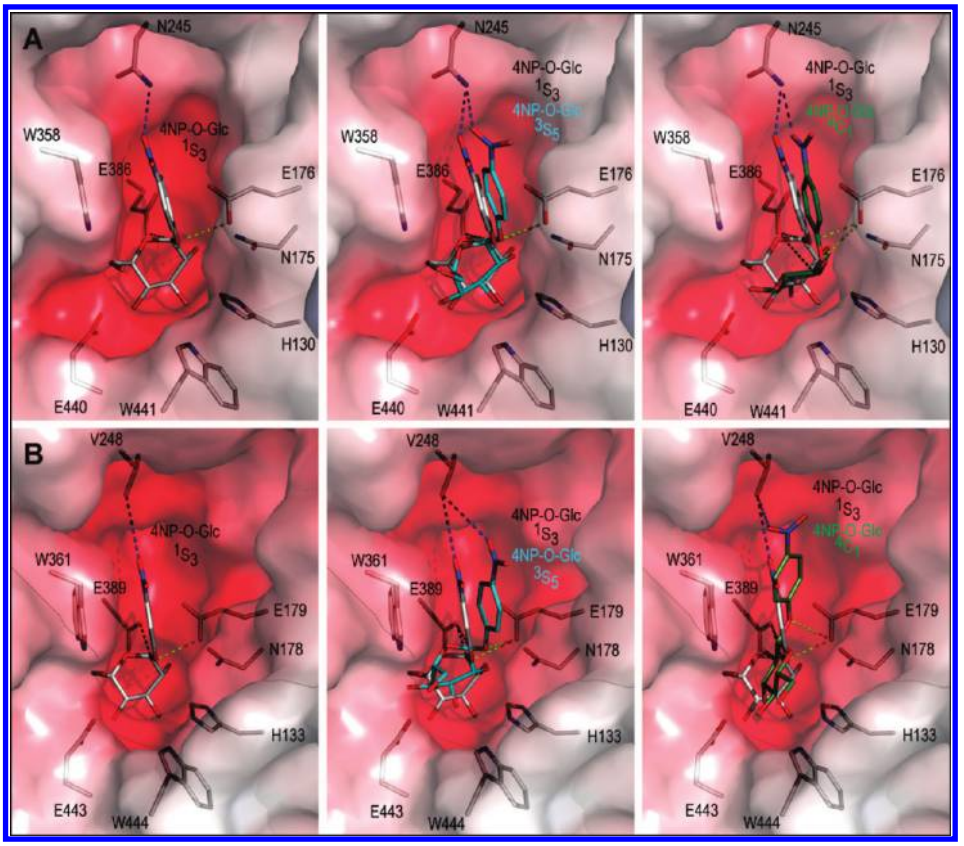

FIGURE 6: Predicted binding positions of 4NP-O-Glc in the active sites of Os3BGlu7 (A) and HvBII (B). The positions of 4NP-O-Glc (A) [left panel, in $^1S_3$ (cpk); middle panel, in $^1S_3$ (cpk) and $^3S_5$ (cpk cyan); right panel, in $^1S_3$ (cpk) and $^4C_1$ (cpk green)] were predicted by GLIDE. The separations between the catalytic nucleophiles E386 (Os3BGlu7) and E389 (HvBII) and acid/base residues E176 (Os3BGlu7) and E179 (HvBII), and the O1 and C1 atoms in 4NP-O-Glc, respectively, are shown as yellow and black dashes. Blue dashes indicate separations between the O atom of the 4NP group and the nearest amino acid residue. Blue and red patches indicate electropositive and electronegative areas contoured at +5 and −10kT/e, respectively. Electrostatic potentials were calculated with Adaptive Poisson−Boltzmann Solver implemented in PyMol.

in the $^4C_1$ (4B) conformer were very similar to those of 3B with both enzymes, whereas the highest values of −7.6 kcal/mol (Os3BGlu7) and −7.3 kcal/mol (HvBII) were calculated for 4NP-S-Man in the $^1S_3$ conformer. The GLIDE scores of 4NP-S-Man in the $^3S_5$ conformer with Os3BGlu7 (−6.0 kcal/mol) and HvBII (−5.7 kcal/mol) ranked relatively close to each other, although 4NP-S-Man bound in the $^4C_1$ conformer was more favored for Os3BGlu7 (−6.6 kcal/mol) than HvBII (−5.7 kcal/mol).

To evaluate the predicted orientations of docked *gluco*- and *manno*-configured O- and S-linked 4NP-glycosides, closer inspections that are summarized in Figures 6−8 were conducted. The best docking positions of 4NP-O-Glc in the $^1S_3$ (1B) geometry indicated that the pyranose rings were located in the intermediate

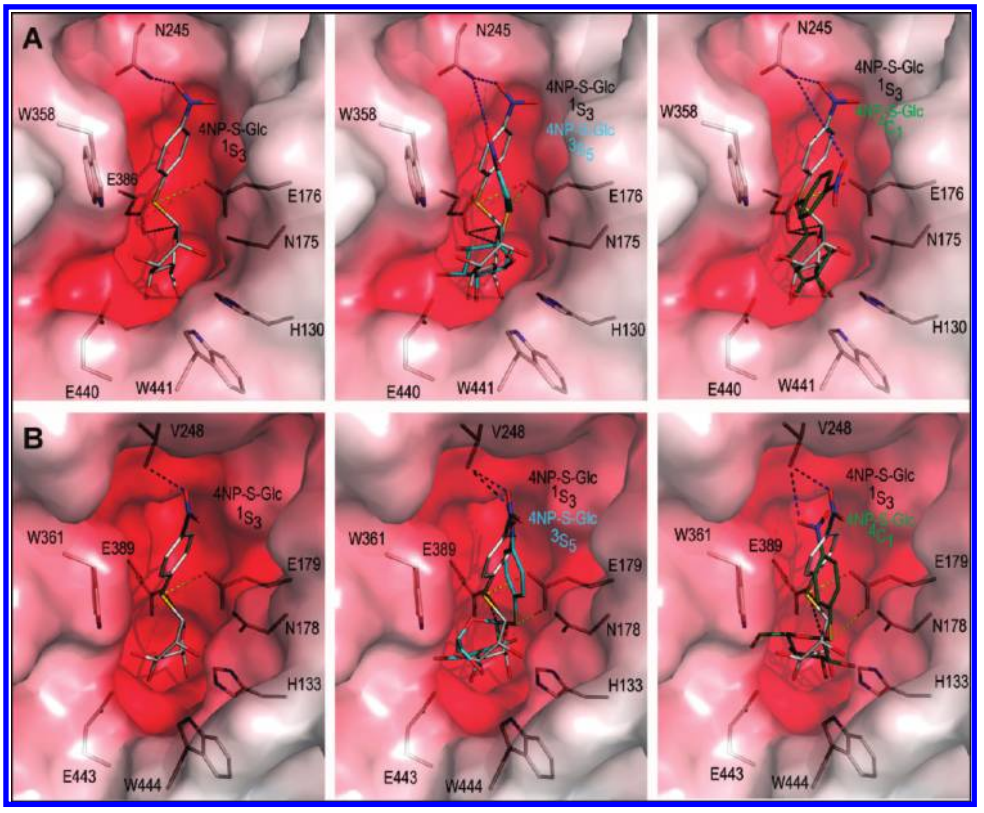

FIGURE 7: Predicted binding positions of 4NP-S-Glc in the active sites of Os3BGlu7 (A) and HvBII (B). In panel A, the positions of 4NP-S-Glc in (left) $^1S_3$ (cpk), (middle) $^1S_3$ (cpk) and $^3S_5$ (cpk cyan), and (right) $^1S_3$ (cpk) and $^4C_1$ (cpk green) were predicted by GLIDE. The separations between the catalytic nucleophiles E386 (Os3BGlu7) and E389 (HvBII) and acid/base residues E176 (Os3BGlu7) and E179 (HvBII), and the S1 and C1 atoms in 4NP-S-Glc, are shown as yellow and black dashes, respectively. Blue dashes indicate the separations between the O atom of the 4NP group and the nearest residue.

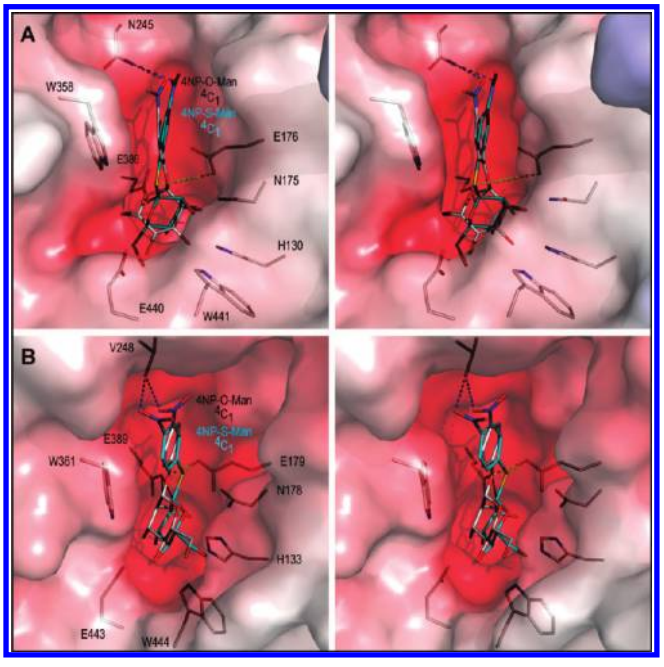

FIGURE 8: Stereoviews of predicted binding positions of 4NP-O-Man and 4NP-S-Man in the active sites of Os3BGlu7 (A) and HvBII (B). The positions of 4NP-O-Man (cpk) and 4NP-S-Man in the $^4C_1$ conformer (cpk cyan) were predicted by GLIDE. The separations between the catalytic nucleophiles E386 (Os3BGlu7), and E389 (HvBII) and acid/base residues E176 (Os3BGlu7) and E179 (HvBII), and the O1 (S1 for 4NP-S-Man) and C1 atoms in 4NP-mannosides, respectively, are shown as yellow and black dashes. Blue dashes indicate the separations between the O atom of the 4NP group and the nearest residue.

positions in the active sites of both enzymes and formed networks of hydrogen bonds with the surrounding residues (Figure 6). The 4NP aglycon of 4NP-O-Glc in $^1S_3$ was in a favorable orientation in the aromatic/hydrophobic funnel, although it did not stretch through its entire length (Figure 6A, right panels). The distances between the anomeric carbons of 4NP-O-Glc and one of the oxygen atoms of the catalytic nucleophiles (EA) Glu386 and Glu389 were 3.2 and 2.9 Å in Os3BGlu7 and HvBII, respectively. The predicted C1$-O_{EA}$ distances in the complexes of Os3BGlu7 and HvBII with 4NP-O-Glc in the $^1S_3$ conformer (black dashes in Figure 6A,B, left panels) suggested that the anomeric carbons were positioned optimally for nucleophilic attacks by the oxygen atoms of catalytic nucleophiles. Further, the glycosidic oxygens in $^1S_3$ were in the reasonable proximities of the catalytic acid/base residues (EB) Glu176 and Glu179, with O1$-O_{EB}$ distances of 3.6 and 3.4 Å in Os3BGlu7 and HvBII, respectively. In addition, the hydrogen atoms of the C2-OH groups pointed to the oxygen atoms of the catalytic acid/base residues. The separations between the protons and the oxygen atoms of EB (HO2$-O_{EB}$) were 1.6 and 3.2 Å for Os3BGlu7 and HvBII, respectively. However, in the case of HvBII, the hydrogen atom was rotated toward Glu389, forming a strong hydrogen bond that was shorter than the HO2$-O_{EB}$ distance of 3.2 Å. These rather short distances suggested that exceptionally strong hydrogen bonds were formed between the participating atoms that may potentially stabilize the enzyme–substrate complex and contribute to the higher affinity of the $^1S_3$ conformer of 4NP-O-Glc to both enzymes, as predicted by GLIDE (Table 2). It was also clear from Table 2 that the affinities of 4NP-O-Glc in the $^3S_5$ and $^4C_1$ geometries were less favorable. Here, the distances between the catalytic residues and C1, O1, and

C2-OH were significantly longer (Table 2). It was remarkable to observe that the 4NP aglycons of 4NP-O-Glc in the $^3S_5$ and $^4C_1$ geometries stretched further through the pocket than that of the $^1S_3$ conformer; in particular, the 4NP aglycon of the $^4C_1$ conformer stretched all the way through the length of the HvBII active site (cf. Figure 6A,B, middle and right panels). While the conformational penalty of the $^1S_3$ conformer was by only 1 kcal/mol lower for Os3BGlu7 than for HvBII, the penalties of the $^3S_5$ and $^4C_1$ conformers of 4NP-O-Glc were clearly higher for HvBII, with energy differences of 8.2 and 7.6 kcal/mol, respectively (cf. ΔE values in Table 2, rows 3 and 4).

In Os3BGlu7, GLIDE predicted a different binding mode for 4NP-S-Glc in the $^1S_3$ geometry (Figure 7). In this instance, the predicted position of the pyranose ring of 4NP-S-Glc overlapped well with that of 2-deoxy-2-fluoroglucoside, observed in the crystal structure of Os3BGlu7 (*16*). However, upon comparison of the positions of the pyranose rings of 4NP-S-Glc with that of 4NP-O-Glc in the $^1S_3$ geometries in both enzymes, the pyranose rings of the S-linked 4NP-glycoside were slightly "out of alignment" in the active sites (Figures 6 and 7, right panels). Moreover, it could be observed that unlike the $^1S_3$ geometry of 4NP-O-Glc, the $^1S_3$ conformer of 4NP-S-Glc in Os3BGlu7 adopted a more "equatorial-like" orientation for the glycosidic linkage with respect to the pyranose ring. However, in HvBII, the $^3S_5$ and $^4C_1$ geometries of 4NP-S-Glc had the glycosidic linkages in equatorial orientations with respect to the pyranose rings, and these linkage orientations seemed to be optimally predisposed for hydrolysis (Figure 7). Here, the distances between C1 of 4NP-S-Glc in $^1S_3$ and O atoms of the catalytic nucleophiles stretched to 4.7 Å in both enzymes, and the distances between S1 of 4NP-S-Glc and O atoms of catalytic acid/base residues were 4.3 and 4.0 Å for Os3BGlu7 and HvBII, respectively. Further, the distances between the C2-OH groups of 4NP-S-Glc and the O atoms of catalytic acid/base residues were 4.4 and 3.1 Å in Os3BGlu7 and HvBII, respectively (Table 2). In summary, the distances between the C1 and S1 atoms of 4NP-S-Glc in $^1S_3$ (2B) conformer and the catalytic residues in both enzymes were significantly longer than those between the C1 and O1 atoms of 4NP-O-Glc in the $^1S_3$ (1B) conformer (Table 2).

Clear differences in the binding of 4NP-S-Glc in the $^3S_5$ geometry were observed between Os3BGlu7 and HvBII (Table 2 and Figure 7, middle panels). In Os3BGlu7, the participating respective distances of 4.6 and 3.4 Å between the EA and EB catalysts and the C1 atoms of 4NP-S-Glc in $^3S_5$ were slightly shorter than those for the $^1S_3$ conformer. Further, the pyranose ring of 4NP-S-Glc in the $^3S_5$ conformer adopted a "flipped-down" orientation compared to that of 4NP-O-Glc in $^1S_3$, as demonstrated by the HO2$-O_{EB}$ distance of 7.1 Å (Table 2). Notably, this conformation posed steric limitations for the interactions between the C1 atom of 4NP-S-Glc in $^3S_5$ and the O1 atom of Glu386 in Os3BGlu7. On the other hand, the C1 atom in the HvBII complex with 4NP-S-Glc in the $^3S_5$ geometry showed a better associative power with EA and EB than 4NP-S-Glc in the $^1S_3$ geometry. Here, the corresponding C1$-O_{EA}$, S1$-O_{EB}$, and HO2$-O_{EB}$ distances were 3.5, 3.4, and 1.5 Å, respectively (Table 2). However, the large conformational penalty of 34 kcal/mol for the HvBII complex with 4NP-S-Glc in the $^3S_5$ geometry most likely contributed to a low GLIDE score of −4.9 kcal/mol for this docking position (Table 2). Finally, binding of 4NP-S-Glc in the $^4C_1$ geometry to both enzymes resulted in scores similar to those that were calculated for 4NP-S-Glc in the $^1S_3$ conformer, although these conformations again adopted the flipped-down pyranose ring orientations. The latter orientations produced longer separations between the C1 atom of 4NP-S-Glc and the O atoms of the EA and EB catalysts and also generated steric hindrances between C1 of 4NP-S-Glc and EA in both enzymes (Figure 7, right panels).

The binding modes of the $^4C_1$ conformers of 4NP-O-Man and 4NP-S-Man in Os3BGlu7 and HvBII that were predicted by GLIDE are illustrated in Figure 8. The stereoviews of binding modes revealed that the two *manno*-configured O- and S-linked 4NP-glycosides adopted very different positions in both enzymes, although the 4NP aglycon moieties of 4NP-O-Man and 4NP-S-Man overlapped reasonably well. As illustrated in Figure 8B, the binding modes of *manno*-configured O- and S-linked 4NP-glycosides in HvBII were almost identical, while in Os3BGlu7, the 4NP aglycons adopted different orientations (Figure 8A). Compared to the $^1S_3$ mannose geometry, the pyranose rings of 4NP-O-Man in the $^4C_1$ geometry in both enzymes adopted flipped-down orientations, where the C1$-O_{EA}$, O1$-O_{EB}$, and HO2$-O_{EB}$ distances were 4.4 and 4.9 Å, 3.5 and 3.9 Å, and 4.3 and 2.5 Å in Os3BGlu7 and HvBII, respectively. The conformational penalty of 4NP-O-Man in the $^4C_1$ conformer favored the HvBII complex over that of Os3BGlu7, as illustrated by the energy difference of nearly 4 kcal/mol (Table 2). On the other hand, the $^4C_1$ conformer of 4NP-S-Man scored slightly better with both enzymes, although the binding modes were dissimilar. In Os3BGlu7, 4NP-S-Man in the $^4C_1$ conformer adopted an orientation that was similar to that of 4NP-O-Glc in the $^1S_3$ conformer, and where the C1 and S1 atoms interacted weakly with EA and EB, as denoted by the C1$-O_{EA}$, S1$-O_{EB}$,and HO2$-O_{EB}$ distances of 4.4, 5.9, and 5.0 Å, respectively (Table 2). However, in HvBII, although the C1 atom of 4NP-S-Man in $^4C_1$ interacted weakly with EA at a C1$-O_{EA}$ distance of 4.7 Å, the S1 atom and the C2-OH group of 4NP-S-Man formed strong interactions with EB with S1$-O_{EB}$ and HO2$-O_{EB}$ distances of 3.1 and 1.7 Å, respectively. Hence, in the HvBII complexes with 4NP-O-Man and 4NP-S-Man in the $^4C_1$ geometry, the axial hydroxyl groups in the C2 positions and the oxygens of EB formed strong interactions, as indicated by their respective separations of 1.7 and 2.5 Å (Table 2 and Figure 8). Noteworthy is the fact that the conformational penalty with 4NP-S-Man in $^4C_1$ was similar for both Os3BGlu7 and HvBII, regardless of the separations between the axial hydroxyl groups in the C2 positions and the EB oxygens (Table 2).

DISCUSSION

A detailed knowledge of binding of β-D-glycosides has paramount importance for understanding of hydrolytic processes. Naturally, the deduction of molecular features of glycosidase−substrate complexes is a complex task as substrates are transformed into products at fast rates. To dissect how binding of β-D-glycosides proceeds at atomistic levels and in particular what specific sugar geometries participate during hydrolysis, mechanism-based inhibitors and substrate analogues have been used to mimic natural glycoside substrates (*46*). In other approaches, variant enzymes containing mutated active site residues have been employed (e.g., ref *47*). The information gained from these studies is critical for glycosidase inhibitor design that has applications in a wide range of biotechnologies, including food and dietary fiber processing and production of pharmaceuticals, nutraceuticals, paper, pulp, wood, and biofuels.

There is mounting evidence that enzymes recognize substrates with a preferential conformational selection mechanism and that

in the absence of substrates, a dynamic equilibrium exists between substrate-free and substrate-bound configurations (*48*). It has been suggested that the most realistic information for substrate binding events is obtained with probes resembling putative transition states (*46*, *49*). Here, binding of transition-state probes is linked to energy gains, resulting from binding of high-energy conformers on a transition-state itinerary of hydrolytic enzymes, where oxocarbonium ion-like-shaped intermediates have been suggested to play key roles (*11*). These events have been investigated predominantly by X-ray diffraction (e.g., refs *15* and (*5052*)), although STD NMR techniques have contributed significantly (*27*, *28*, *53*).

Against this background, the goal of our study was to shed light on the structural basis of binding of S- and O-linked *gluco*- and *manno*-configured aryl-β-D-glycosides to the Os3BGlu7 and HvBII enzymes that preferentially hydrolyze β-D-glucoside and β-D-mannoside substrates, respectively (*3*−*7*). Our aim was also to understand how chemical and structural features in substrates and enzymes' active sites underlie the substrate specificity of these enzymes that are classified in the GH-A clan of CAZy classification (*1*).

We first determined and compared kinetic parameters of inhibition (K_i) and hydrolysis (K_m) with S- and O-linked *gluco*- and *manno*-configured aryl-β-D-glycosides (Table 1). The comparisons of the kinetic data of HvBII and Os3BGlu7, using the corresponding O-glycoside substrates, revealed that the observed trends in K_i values of the thio analogues did not necessarily follow those in the K_m values. For example, with Os3BGlu7, where both thio inhibitors were almost equally effective, the K_m values for 4NP-O-Glc and 4NP-O-Man differed by a factor of ~6. This conclusion was also valid for HvBII, where, while 4NP-S-Glc was nearly 3-fold more potent than 4NP-S-Man, the K_m value for the O-linked glucoside was 2 times higher than that for 4NP-O-Man (Table 1). Overall, the inhibition experiments clearly demonstrated that HvBII was far more sensitive to the inhibition by 4NP-S-Glc and 4NP-S-Man than Os3BGlu7 and that the K_m and K_i values with O- and S-linked *gluco*- and *manno*-configured aryl-β-D-glycosides could not be correlated.

To reconcile the differences in binding of the O- and S-linked aryl glycosides that serve as respective substrates and inhibitors in Os3BGlu7 and HvBII, STD NMR and trNOESY investigations coupled with QM/MM modeling and docking experiments were undertaken. Here, we aimed to investigate precise conformations of S-linked *gluco*- and *manno*-configured aryl-β-D-glycosides in bound states, and if the distortions from the $^4C_1$ ground states could be observed by STD NMR and trNOESY spectroscopy. These studies were complemented with predictive molecular modeling approaches. We surmised that these two approaches could provide useful insights, in particular, when crystal structures of inhibitor−ligand complexes are not available. The former technique has become a powerful tool in recent years for the characterization of binding of mechanistic probes to proteins (e.g., refs *27* and *28*) and relies on saturation transfer from protein to ligand molecules. Thus, when a protein is selectively irradiated, the ligand between bound and free forms also becomes saturated in a bound state. Subtraction of the spectra acquired with off-resonance irradiation readily reveals conformations of a bound ligand, and the differential STD effects within a ligand molecule provide the information about the proximity of individual protons present in the vicinity of a protein. The advantage of this technique is that it is rapid and does not require isotope labeling of proteins or excessively large quantities of protein.

The STD NMR and trNOESY experiments were set up in several stages. As previously shown (*28*), when ligands bind weakly and when exchange rates between free and bound states occur at reasonably fast rates, trNOESY signals could provide adequate means for determining conformations of glycosides. After the S-linked *gluco*- and *manno*-configured aryl-β-D-glycosides were incubated with HvBII, strong negative NOE cross-peaks were observed, indicating binding of inhibitors to the enzymes, in contrast to the free states of inhibitors. Via the trNOESY experiments with HvBII, we could unambiguously deduce conformational changes of the six-member rings of 4NP-S-Glc and 4NP-S-Man. Upon comparison of the experimental interproton distances of bound 4NP-S-Glc with those measured in the MM3*-minimized geometries, we concluded that 4NP-S-Glc adopted the $^3S_5$ or $^1S_3$ skew boat geometry, while 4NP-S-Man did not deviate from a starting low-energy $^4C_1$ geometry. The analogous STD NMR and trNOESY analyses for 4NP-S-Glc and 4NP-S-Man bound to Os3BGlu7 were also performed and showed that both thioglycosides remained in the ground $^4C_1$ conformations and that major saturation transfers were observed only on aromatic protons. The latter conclusions were supported by inhibition kinetics indicating that both β-D-thioglycosides were rather weak inhibitors (Table 1). The existence of no major contacts with the enzyme, in principle, suggests that no distortion of the ring is taking place upon binding. Further, the lack of observable NOESY cross-peaks for the sugar part during binding of 4NP-S-Glc and 4NP-S-Man to Os3BuGlu7 may also suggest that future experiments with other inhibitors such as S-alkyl or S-benzyl derivatives are necessary and will ultimately clarify if the distortions of 4NP-S-glycosides upon binding to Os3BGlu7 occur.

The STD NMR and trNOESY experiments were complemented with QM/MM docking computations. During the docking procedure, the geometry of active site side chains was optimized, and this approach coupled with the QM-derived partial charges provided a basis for binding predictions by molecular docking. For these computations, we used a crystal structure of Os3BGlu7 (PDB entry 2RGM), while a homology model was constructed for HvBII, in the absence of its 3D structure. During the docking procedure, the orientations of the key amino acid residues in both proteins were sufficiently relaxed for the docked molecules to adjust. Although caution should be exercised in interpreting the computational data using homology models, as subtle errors in modeled HvBII could lead to erroneous miscalculations of docked positions and docking energies, in our experience the docking procedure using reliable homology models leads to reasonable predictions. Nevertheless, the use of the same models of, e.g., variant enzymes, where large conformational changes or variations in partial charges of amino acid residues occur, must be interpreted carefully because they could lead to erroneous prediction of binding affinities.

For docking of β-D-glycosides, we used as a guide an experimentally determined position of 2-deoxy-2-fluoroglucoside in Os3BGlu7 (*16*). When the characteristics of the active sites of Os3BGlu7 and HvBII were compared, it became obvious that they contained a plethora of charged and hydrophobic residues, where the catalytic nucleophiles Glu386 (Os3BGlu7) and Glu389 (HvBII) (*4*, *16*) at subsite −1 were expected to form covalent linkages with the anomeric carbons of the substrates during formation of glycosyl−enzyme intermediates. The other important catalysts in the active sites of Os3BGlu7 and HvBII are the catalytic acid/base residues Glu176 (Os3BGlu7) and Glu179

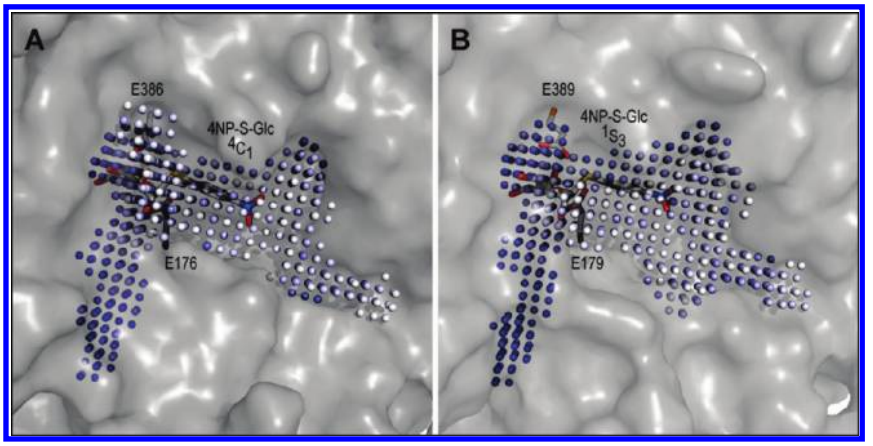

FIGURE 9: Shapes and buriedness of active site funnels of Os3BGlu7 and HvBII. The positions of 4NP-S-Glc (cpk) are shown in preferred geometries, $^4C_1$ for Os3BGlu7 (A) or $^1S_3$ for HvBII (B), as identified by STD NMR. The catalytic nucleophiles E386 (Os3BGlu7) and E389 (HvBII) and acid/base residues E176 (Os3BGlu7) and E179 (HvBII) are shown in cpk. Binding sites are given in the PocketPicker descriptors (*38*), with darker spheres indicating greater buriedness.

(HvBII) that, according to the canonical mechanism, should protonate glycosidic oxygens during hydrolysis. Moreover, in Os3BGlu7, the catalytic site is surrounded by a series of bulky hydrophobic/aromatic residues, namely, Trp433 and Trp441, and other residues such as Trp358 and Tyr315 that form a hydrophobic funnel (*16*). Here, a particular emphasis is placed on Trp433 positioned at the bottom of the active site pocket that mediates stacking interactions with the pyranose ring of 2-deoxy-2-fluoroglucoside (*16*).

One would expect that these interactions might be one of the major forces that keep substrates in favorable orientations for a nucleophilic attack. Further, at subsite 1, residues Ile179, Leu183, Tyr315, and Trp358 formed a hydrophobic funnel that presumably could accommodate the aglycon moieties of substrates. Thus, it would be expected that a specific and characteristic shape, buriedness, and geometry of active sites are required for particular conformations of substrates to bind in the active site regions. Here, a comparison of shape properties, using PocketPicker descriptors (*38*), indicated that both enzymes had very similar shapes, depths, and geometries of active site funnels (Figure 9). One would also expect that significant differences in conformations and charges in O- and S-linked 4NP-Glc and 4NP-Man might have serious consequences for the shapes of electrostatic surfaces of glycosides that could influence binding modes of substrates in enzymes' active sites, in particular those in subsites −1 and 1. These features are summarized in Figures 5 and 9 and in Table S3 of the Supporting Information, collectively indicating that O- and S-linked aryl-β-D-glycosides exhibit certain characteristic electrostatic potentials, and that these potentials are dependent on geometries of the individual pyranose rings. In particular, the data in Table S3 of the Supporting Information indicated that significant differences in the ESP charge distributions in the O- and S-linked glycosides occurred in the vicinity of their anomeric C1 atoms. It was therefore not unexpected that, after the glycosidic oxygens were replaced with sulfurs, the ESP charges on the C1 atoms changed from the positive values to the negative ones in all conformers (Table S3 of the Supporting Information). On the other hand, the overall ESP charges on the X1 and O4 atoms became less negative (Table S3 of the Supporting Information).

A few observations from the modeling experiments are worth analyzing. It seemed that in addition to characteristic positions of the S-linked *gluco*- and *manno*-configured aryl-β-D-glycoside conformers in the active site funnels, defined by their separations from the respective active site residues, the overall sidedness of the pyranose ring orientations varied. The so-called flipped-down $^4C_1$ conformations of 4NP-S-Glc and 4NP-O-Man were adopted in Os3BGlu7 and HvBII (Figures 6 and 8), and a similar orientation was also seen in the $^3S_5$ conformer of 4NP-S-Glc that bound to Os3BGlu7 (Figure 7A, middle panel), compared to a 2-deoxy-2-fluoroglucoside moiety in the covalent complex of Os3BGlu7 (*16*). These flipped-down conformations resulted in unusually long C2-OH$-O_{EB}$ separations of more than 7 Å in Os3BGlu7 (Table 2), except for that of 4NP-O-Man, and were also associated with longer separations between β-D-glycosides and respective active site residues EA and EB. This observation indicated that both enzymes could select incorrect orientations of incoming substrates that bind less favorably in their catalytic funnels. The importance of hydrogen bonds between the C2-OH group and catalytic residues was emphasized in a theoretical study of the catalytic mechanisms of β-D-glycoside hydrolases, where Bras and co-workers (*52*) concluded that the C2-OH$-O_{EA}$ hydrogen bond is responsible for a low-energy activation barrier in the *E. coli* β-galactosidase catalytic mechanism.

Further, scoring algorithms that evaluate the accuracy of docking (Figures 6−8 and Table 2) and that could distinguish between various binding modes of ligands deserve mentioning, although the accuracy of predicting precise affinities in quantitative terms could be relatively low (*44*, *54*). Nevertheless, the data from our modeling experiments clearly demonstrated that binding behavior of 4NP-S-Glc and 4NP-S-Man differed between the two plant enzymes. In was noteworthy that the bound O- and S-linked *gluco*- and *manno*-configured aryl-β-D-glycosides did not adopt necessarily their lowest-energy conformations in bound states (Table 2). To estimate the strain energy imposed by the active site environments, we calculated the energy differences of bound aryl-β-D-glycosides at the M05-2X/6-31+G* level of theory. These energy differences arose from the differences between their local minima in free and bound states (Table 2). From these values, one could infer how binding of O- and S-linked *gluco*- and *manno*-configured aryl-β-D-glycosides in the higher-energy states influences the hydrolytic activation barrier.

Finally, it has been suggested for the members of the GH26 group of β-D-mannanases and (1,3;1,4)-β-D-glucan endohydrolases, which like the β-D-glucosidases and β-D-mannosidases

studied here are the members of clan GH-A, that while the interactions around the C1 and C2-OH groups were similar, environments around C3-OH groups could contribute to the specificity of the reaction coordinate (*55*). The authors further suggested that although the chemistry of the bound sugar is important, it does not dominate substrate specificity; whereas for *manno*-configured substrates, both $B_{2,5}$ and $^{3}H_{4}$ transition states participate, for *gluco*-configured substrates, the $^{4}H_{3}$ and $B^{2,5}$ transition states participate (*55*). Subsequently, a Michaelis complex of a GH2 β-D-mannosidase BtMan2A was published, which suggested that a boatlike transition state develops on a $^{1}S_{5}-B_{2,5}-{}^{O}S_{2}$ itinerary in this class of hydrolases (*56*). However, in the work described here, we concluded that other conformations, such as those participating in the $^{1}S_{5}-B_{2,5}-{}^{O}S_{2}$ itinerary for BtMan2A, are highly unlikely.

Our computational data indeed showed that the so-called flipped-down $^{4}C_{1}$ conformation of 4NP-O-Man was adopted in Os3BGlu7 and HvBII. On the other hand, the QM/MM modeling experiments indicated that the most favorable geometry for 4NP-O-Man with both Os3BGlu7 and HvBII was $^{1}S_{3}$ (Table 2). Here we did not test the significance of $^{1}S_{5}$ geometry, although we presume that geometrical interconversions between $^{1}S_{5}$ and $^{1}S_{3}$ should be less significant than those between $^{3}S_{5}$ and $^{1}S_{3}$, and thus, the $^{1}S_{3}$ conformer could be considered as an intermediate between the $^{3}S_{5}$ ($B_{3,O}$) and $^{1}S_{5}$ conformers. The $^{1}S_{3}$ geometry was also identified in 4NP-O-Glc with both β-D-glycosidases through the QM modeling and docking experiments, although STD NMR and trNOESY experiments confirmed its existence only with 4NP-S-Glc. To complicate the matters even further, it has recently been reported with a β-D-glucosidase from a soil metagenome library (*57*) that in addition to the glycon, the nature of the aglycon could contribute to substrate specificity. Similar observations were previously reported with a maize β-glucosidase (*20*) and diverse β-D-mannanases (*58*).

In summary, STD NMR and trNOESY experiments in conjunction with molecular docking simulations provided information about binding of S- and O-linked *gluco*- and *manno*-configured aryl-β-D-glycosides to rice Os3BGlu7 and barley HvBII that operate predominantly as a β-D-glucosidase and β-D-mannosidase, respectively. Kinetic analyses with 4NP-S-Glc and 4NP-S-Man indicated that the inhibitions were competitive. The STD NMR and trNOESY experiments revealed that 4NP-S-Glc and 4NP-S-Man bound weakly in $^{4}C_{1}$ conformations to Os3BGlu7, 4NP-S-Glc adopted the $^{3}S_{5}$ or $^{1}S_{3}$ conformation, and 4NP-S-Man preferred $^{4}C_{1}$ geometry with HvBII. The docking and modeling studies predicted that 4NP-O-Glc, 4NP-O-Man, and 4NP-S-Man bound preferentially in the $^{1}S_{3}$ geometries to both enzymes, contrary to 4NP-S-Glc that could adopt a range of geometries ($^{1}S_{3}$, $^{3}S_{5}$, or $^{4}C_{1}$). Although NMR, kinetic, and QM/MM examinations presented in this study provide valuable information about the conformations of sugars bound by the two plant β-D-glycosidases with distinct substrate specificities, we further surmise that the depth of information could be further enhanced via X-ray crystallography, and thus the amalgamation of the four techniques would ideally represent the most powerful approach for evaluation of binding affinities (*60*).

We conclude that in the plant β-D-glucoside hydrolase Os3BGlu7 and β-D-mannoside hydrolase HvBII a combination of determinants is likely to play roles in substrate recognition, such as (i) the inherent conformational and spatial flexibilities of *gluco*- and *manno*-configured substrates in the enzymes' active sites, (ii) the subtle spatial differences in the disposition of active site residues and their capacities to form interactions with specific groups of substrates, and (iii) the small variations in charge distributions and shapes of the catalytic sites. We anticipate that the combination of these determinants may collectively drive the key interactions between the active site residues and *gluco*- and *manno*-configured substrates and underlie the enzymes' substrate specificities.

ACKNOWLEDGMENT

J.C., L.C., and J.J.-B. thank J. J. Hernández-Gay for helpful discussions.

SUPPORTING INFORMATION AVAILABLE

Supplementary Tables 1−3. This material is available free of charge via the Internet at http://pubs.acs.org.

REFERENCES

1. Cantarel, B. L., Coutinho, P. M., Rancurel, C., Bernard, T., Lombard, V., and Henrissat, B. (2009) The carbohydrate-active enzymes database (CAZy): An expert resource for glycogenomics. *Nucleic Acids Res. 37*, D233–D238.
2. Hrmova, M., and Fincher, G. B. (2009) Depolymerizing enzymes. In Chemistry, Biochemistry and Biology of (1,3)-β-D-Glucans and Related Polysaccharides (Bacic, T., Fincher, G. B., and Stone, B. A., Eds.) pp 119−170, Academic Press and Elsevier Inc., San Diego.
3. Hrmova, M., Harvey, A. J., Wang, J., Shirley, N. J., Jones, G. P., Stone, B. A., Høj, P. B., and Fincher, G. B. (1996) Barley β-D-glucan exohydrolases with β-D-glucosidase activity. Purification and determination of primary structure from a cDNA clone. *J. Biol. Chem. 271*, 5277–5286.
4. Hrmova, M., MacGregor, E. A., Biely, P., Stewart, R. J., and Fincher, G. B. (1998) Substrate binding and catalytic mechanism of a barley β-D-glucosidase/(1,4)-β-D-glucan exohydrolase. *J. Biol. Chem. 273*, 11134–11143.
5. Hrmova, M., Burton, R. A., Biely, P., Lahnstein, J., and Fincher, G. B. (2006) Hydrolysis of (1,4)-β-D-mannans in barley (*Hordeum vulgare* L.) is mediated by a concerted action of a (1,4)-β-D-mannan endohydrolase and a β-D-mannosidase. *Biochem. J. 399*, 77–90.
6. Kuntothom, T., Luang, S., Fincher, G. B., Opassiri, R., Hrmova, M., and Ketudat Cairns, J. R. (2008) Closely related barley and rice family GH1 glycosyl hydrolases with β-D-glucosidase and β-D-mannosidase activities. *Arch. Biochem. Biophys. 491*, 85–95.
7. Opassiri, R., Hua, Y., Wara-aswapati, O., Akiyama, T., Svasti, J., Esen, A., and Ketudat Cairns, J. R. (2004) β-Glucosidase, exo-β-glucanase and pyridoxine transglucosylase activities of rice BGlu1. *Biochem. J. 379*, 125–131.
8. Marana, S. R. (2006) Molecular basis of substrate specificity in family 1 glycoside hydrolases. *IUMB Life 58*, 6–73.
9. Vocadlo, D. J., and Davies, G. J. (2008) Mechanistic insights into glycosidase chemistry. *Curr. Opin. Chem. Biol. 12*, 539–555.
10. Burmeister, W. P., Cottaz, S., Driguez, H., Iori, R., Palmieri, S., and Henrissat, B. (1997) The crystal structures of *Sinapis alba* myrosinase and a covalent glycosyl-enzyme intermediate provide insights into the substrate recognition and active-site machinery of an S-glycosidase. *Structure 5*, 663–675.
11. Zechel, D. L., and Withers, S. G. (2001) Dissection of nucleophilic and acid-base catalysis in glycosidases. *Curr. Opin. Chem. Biol. 5*, 643–649.
12. Vallmitjana, M., Ferrer-Navarro, M., Planell, R., Abel, M., Querol, E., Planas, A., and Pérez-Pons, J.-A. (2001) Mechanism of the family β-glucosidase from *Streptomyces* sp.: Catalytic residues and kinetic studies. *Biochemistry 40*, 5975–5982.
13. Ly, H. D., and Withers, S. G. (1999) Mutagenesis of glycosidases. *Annu. Rev. Biochem. 68*, 487–522.
14. Cicek, M., Blanchard, D., Bevan, D. R., and Esen, A. (2000) The aglycone specificity-determining sites are different in 2,4-dihydroxy-7-methoxy-1,4-benzoxazin-3-one (DIMBOA)-glucosidase (maize β-glucosidase) and dhurrinase (sorghum β-glucosidase). *J. Biol. Chem. 275*, 20002–20011.

15. Czjzek, M., Cicek, M., Zamboni, V., Bevan, D. R., Henrissat, B., and Esen, A. (2000) The mechanism of substrate (aglycone) specificity in β-glucosidases is revealed by crystal structures of mutant maize β-glucosidase-DIMBOA, -DIMBOAGlc, and -dhurrin complexes. *Proc. Natl. Acad. Sci. U.S.A. 97*, 13555–13560.
16. Chuenchor, W., Pengthaisong, S., Robinson, R. C., Jirundon, Y., Esen, A., Chen, C.-J., Opassiri, R., Svasti, J., and Ketudat Cairns, J. R. (2008) Structural insights into rice BGlu1 β-glucosidase oligosaccharide hydrolysis and transglycosylation. *J. Mol. Biol. 377*, 1200–1215.
17. Street, I. P., Kempton, J. B., and Withers, S. G. (1992) Inactivation of a β-glucosidase through the accumulation of a stable 2-deoxy-2-fluoro-β-D-glucopyranosyl-enzyme intermediate: A detailed investigation. *Biochemistry 31*, 9970–9978.
18. Bause, E., and Legler, G. (1980) Isolation and structure of a tryptic glycopeptide from the active site of β-glucosidase A_3 from *Aspergillus wentii*. *Biochim. Biophys. Acta 626*, 459–465.
19. Aguilar, C. F., Sanderson, I., Moracci, M., Ciaramella, M., Nucci, R., Rossi, M., and Pearl, L. H. (1997) Crystal structure of the β-glycosidase from the hyperthermophilic archeon *Sulfolobus solfataricus*: Resilience as a key factor in thermostability. *J. Mol. Biol. 271*, 789–802.
20. Verdoucq, L., Moriniere, J., Bevan, D. R., Esen, A., Vasella, A., Henrissat, B., and Czjzek, M. (2004) Structural determinants of substrate specificity in family 1 β-glucosidases: Novel insights from the crystal structure of sorghum dhurrinase-1, a plant β-glucosidase with strict specificity, in complex with its natural substrate. *J. Biol. Chem. 279*, 31796–31803.
21. Sulzenbacher, G., Driguez, H., Henrissat, B., Schülein, M., and Davies, G. J. (1996) Structure of the *Fusarium oxysporum* endoglucanase I with a nonhydrolyzable substrate analogue: Substrate distortion gives rise to the preferred axial orientation for the leaving group. *Biochemistry 35*, 15280–15287.
22. Hrmova, M., De Gori, R., Smith, B. J., Fairweather, J. K., Driguez, H., Varghese, J. N., and Fincher, G. B. (2002) Structural basis for a broad specificity in higher plant β-D-glucan glucohydrolases. *Plant Cell 14*, 1033–1052.
23. Money, V., Cartmell, A., Guerreiro, C. I. P. D., Ducros, V. M.-A., Fontes, C. M. G. A., Gilbert, H. J., and Davies, G. J. (2008) Probing the β-1,3:1,4 glucanase, *Ct*Lic26A, with a thio-oligosaccharide and enzyme variants. *Org. Biomol. Chem. 6*, 851–853.
24. Opassiri, R., Ketudat Cairns, J. R., Akiyama, T., Wara-aswapati, O., Svasti, J., and Esen, A. (2003) Characterization of a rice β-glucosidase highly expressed in flower and germinating shoot. *Plant Sci. 165*, 627–638.
25. Blanc-Muesser, M., Defaye, J., and Driguez, H. (1978) Syntheses stereoselectives de 1-thioglucosides. *Carbohydr. Res. 67*, 305–328.
26. Chuenchor, W., Pengthaisong, S., Yuvaniyama, J., Opassiri, R., Svasti, J., and Ketudat Cairns, J. R. (2006) Purification, crystallization and preliminary X-ray analysis of rice BGlu1 β-glucosidase with and without 2-deoxy-2-fluoro-β-D-glucoside inhibitor. *Acta Crystallogr. F62*, 798–801.
27. Vogtherr, M., and Peters, T. (2000) Application of NMR based binding assays to identify key hydroxyl groups for intermolecular recognition. *J. Am. Chem. Soc. 122*, 6093–6099.
28. Clavel, C., Canales, A., Gupta, G., Cañada, F. J., Penadés, S., Suriola, A., and Jiménez-Barbero, J. (2007) NMR investigation of the bound conformation of natural and synthetic oligomannosides to banana lectin. *Eur. J. Org. Chem. 10*, 1577–1585.
29. Thompson, J. D., Gibson, T. J., Plewniak, F., Jeanmougin, F., and Higgins, D. G. (1997) The CLUSTAL_X windows interface: Flexible strategies for multiple sequence alignment aided by quality analysis tools. *Nucleic Acids Res. 24*, 4876–4882.
30. Kim, D. E., Chivian, D., and Baker, D. (2004) Protein structure prediction and analysis using the Robetta server. *Nucleic Acids Res. 32* (Suppl. 2), W256–W231.
31. Sali, A., and Blundell, T. L. (1993) Comparative protein modelling by satisfaction of spatial restraints. *J. Mol. Biol. 234*, 779–815.
32. Laskowski, R. A., MacArthur, M. W., Moss, D. S., and Thornton, J. M. (1993) PROCHECK: A program to check the stereochemical quality of protein structures. *J. Appl. Crystallogr. 26*, 283–291.
33. Vriend, G. (1990) WHAT IF: A molecular modeling and drug design program. *J. Mol. Graphics 8*, 52–56.
34. Lüthy, R., Bowie, J. E., and Eisenberg, D. (1992) Assessment of protein models with three-dimensional profiles. *Nature 356*, 83–85.
35. Sippl, M. J. (1993) Recognition of errors in 3-dimensional structures of proteins. *Proteins: Struct., Funct., Bioinf. 17*, 355–362.
36. Sumathi, K., Ananthalakshmi, P., Md Roshan, M. B. A., and Sekar, K. (2006) 3dSS: 3D structural superposition. *Nucleic Acids Res. 34*, W128–W134.
37. DeLano, W. (2009) The PyMOL Molecular Graphics System, DeLano Scientific LLC, San Carlos, CA.
38. Weisel, M., Proschak, E., and Schneider, G. (2007) PocketPicker: Analysis of ligand-binding sites with shape descriptors. *Chem. Cent. J. 1*, 7.
39. MacroModel, version 9.6 (2008) Schrödinger, LLC, New York.
40. Zhao, Y., Schultz, N. E., and Truhlar, D. G. (2005) Exchange-correlation functional with broad accuracy for metallic and nonmetallic compounds, kinetics, and noncovalent interactions. *J. Chem. Phys. 123*, 161103.
41. Zhao, Y., Schultz, N. E., and Truhlar, D. G. (2006) Design of density functionals by combining the method of constraint satisfaction with parametrization for thermochemistry, thermochemical kinetics, and noncovalent interactions. *J. Chem. Theory Comput. 2*, 364–382.
42. Zheng, J., Zhao, Y., and Truhlar, D. G. (2007) Representative benchmark suites for barrier heights of diverse reaction types and assessment of electronic structure methods for thermochemical kinetics. *J. Chem. Theory Comput. 3*, 569–582.
43. Jorgensen, W. L., Maxwell, D. S., and Tirado-Rives, J. (1996) Development and testing of the OPLS all-atom force field on conformational energetics and properties of organic liquids. *J. Am. Chem. Soc. 118*, 11225–11236.
44. Friesner, R. A., Banks, J. L., Murphy, R. B., Halgren, T. A., Klicic, J. J., Mainz, D. T., Repasky, M. P., Knoll, E. H., Shelley, M., Perry, J. K., Shaw, D. E., Francis, P., and Shenkin, P. S. (2004) Glide: A new approach for rapid, accurate docking and scoring. 1. Method and assessment of docking accuracy. *J. Med. Chem. 47*, 1739–1749.
45. Tvaroška, I., and Carver, J. P. (1996) *Ab initio* molecular orbital calculation of carbohydrate model compounds. 5. Anomeric, exo-anomeric, and reverse anomeric effects in C-, N-, and S-glycosyl compounds. *J. Phys. Chem. 100*, 11305–11313.
46. Rempel, B. P., and Withers, S. G. (2008) Covalent inhibitors of glycosidases and their applications in biochemistry and biology. *Glycobiology 18*, 570–586.
47. Blanchard, J. E., and Withers, S. G. (2001) Rapid screening of the aglycone specificity of glycosidases: Applications to enzymatic synthesis of oligosaccharides. *Chem. Biol. 8*, 627–633.
48. Davulcu, O., Flynn, P. F., Chapman, M. S., and Skalicky, J. J. (2009) Intrinsic domain and loop dynamics commensurate with catalytic turnover in an induced-fit enzyme. *Structure 17*, 1356–1367.
49. Ermert, P., Rupitz, K., Vasella, A., Weber, M., and Withers, S. G. (1993) Transition state analogue inhibitors of glycosidases are configurationally selective: A study with nojiritetrazoles, a new class of glycosidase inhibitors. *Carbohydr. Res. 250*, 113–128.
50. Hrmova, M., Streltsov, V. A., Smith, B. J., Vasella, A., Varghese, J. N., and Fincher, G. B. (2005) Structural rationale for low nanomolar binding of transition state mimics to a family GH3 β-D-glucan glucohydrolase from barley. *Biochemistry 44*, 16529–16539.
51. Gloster, T. M., Meloncelli, P., Stick, R. V., Zechel, D., Vasella, A., and Davies, G. J. (2007) Glycosidase inhibition: An assessment of the binding of 18 putative transition-state mimics. *J. Am. Chem. Soc. 129*, 2345–2354.
52. Bras, N. F., Moura-Tamares, A., Fernandes, P. A., and Ramos, M. J. (2008) Mechanistic studies on the formation of glycosidase-substrate and glycosidase-inhibitor covalent intermediates. *J. Comput. Chem. 29*, 2565–2574.
53. Martin-Pastor, M., Vega-Vázquez, M., De Capua, A., Canales, A., Andre, S., Gabius, H. J., and Jiménez-Barbero, J. (2006) Enhanced signal dispersion in saturation transfer difference experiments by conversion to a 1D-STD-homodecoupled spectrum. *J. Biomol. NMR 36*, 103–109.
54. Englebienne, P., Fiaux, H., Kuntz, D. A., Corbeil, C. R., Gerber-Lemaire, S., Rose, D. R., and Moitessier, N. (2007) Evaluation of docking programs for predicting binding of Golgi α-mannosidase II inhibitors: A comparison with crystallography. *Proteins 69*, 160–176.
55. Money, V. A., Smith, N. L., Scaffidi, A., Stick, R. V., Gilbert, H. J., and Davies, G. J. (2006) Substrate distortion by a lichenase highlights the different conformational itineraries harnessed by related glycoside hydrolases. *Angew. Chem., Int. Ed. 45*, 5136–5140.

56. Offen, W. A., Zechel, D. L., Withers, S. G., Gilbert, H. J., and Davies, G. J. (2009) Structure of the Michaelis complex of β-mannosidase, Man2A, provides insight into the conformational itinerary of mannoside hydrolysis. *Chem. Commun.,* 2484–2486.
57. Nam, K. H., Sung, M. W., and Hwang, K. Y. (2010) Structural insights into the substrate specificity of β-glucosidase. *Biochem. Biophys. Res. Commun. 391*, 1131–1135.
58. Tailford, L. E., Ducros, V. M., Flint, J. E., Roberts, S. M., Morland, C., Zechel, D. L., Smith, N., Bjørnvad, M. E., Borchert, T. V., Wilson, K. S., Davies, G. J., and Gilbert, H. J. (2009) Understanding how diverse β-mannanases recognize heterogeneous substrates. *Biochemistry 48*, 7009–7018.
59. Fersht, A. (1999) Structure and Mechanism in Protein Science, pp 1−631, W. H. Freeman and Co., New York.
60. Hrmova, M., and Fincher, G. B. (2009) Functional genomics and structural biology in the definition of gene function. In Methods in Molecular Biology: Plant Genomics (Somers, D., Langridge, P., and Gustafson, P., Eds.) Vol. 513, pp 175−198, Humana Press Inc., Totowa, NJ.